

JOURNAL PRE-PROOF



**CARBONATIZATION AND SILICIFICATION OF PERIDOTITES
WITHIN THE VEZIRLER OPHIOLITIC MÉLANGE (KULA-
MANISA, WESTERN TÜRKIYE): A NATURAL ANALOGUE FOR
CO₂ SEQUESTRATION**

Mehmet Akbulut, Murat Tokcaer, Zeynep Büçkün

To appear in OFIOLITI

DOI: <https://doi.org/10.4454/ofioliti.v49i2.569>

Received date: 16 December 2023
Accepted date: 26 March 2024
First published online: 21 April 2023

CARBONATIZATION AND SILICIFICATION OF PERIDOTITES WITHIN THE VEZIRLER OPHIOLITIC MÉLANGE (KULA-MANISA, WESTERN TÜRKİYE): A NATURAL ANALOGUE FOR CO₂ SEQUESTRATION

Mehmet Akbulut^{1,1}, Murat Tokcaer¹, Zeynep Büçkün¹

⁽¹⁾Dokuz Eylül University, Faculty of Engineering, Department of Geological Engineering, Buca-İzmir, TÜRKİYE

Keywords: Carbonatization, serpentinized peridotites, listvenite, CO₂ storage, Vezirler Mélange, Kula, Western Anatolia.

ABSTRACT

This study presents a detailed mineralogical description of carbonatization and silicification products derived from a serpentinite outcrop within the Vezirler ophiolitic mélange near Kula (Manisa, Western Türkiye). The investigated outcrop displays a significant alteration profile from bottom to top, including carbonatized and silicified serpentinite (CS-Srp), a coalesced carbonate nodule zone (Cnz), and an iron-oxide stained silica-carbonate alteration crust (Fsc). The blackish green to green coloured, very slightly carbonatized or non-carbonatized parts of the serpentinite is mainly made of serpentine polymorphs, bastite transformed orthopyroxene, chromites, iron-oxides, and andradite. Minor carbonatization is observed with dolomite and hematite-bearing coronas around andradite in contact with the serpentine polymorphs. In contrast, CS-Srp comprises hydromagnesite-hydrotalcite nodules within a greenish-gray serpentinite matrix. Near the Cnz contact, discrete magnesite nodules are present, while the Cnz consist of agglomerated magnesite nodules. Fsc above the Cnz, contains magnesite nodules and dolomite-silica stockwork in the lower segment and only dolomite-silica stockwork in the upper segment. The rhythmically zoned magnesites suggest changing reactant phases during carbonatization, influenced by temperature, Si solubility, X_{CO₂}, reactive surface area, and water/rock ratio. Tectonic control is indicated by the contact between Fsc and Cnz, suggesting a roughly N60W strike and a low-angle NE dipping trend (<10°). The minimal presence of Ca-bearing minerals in the alteration paragenesis suggests a Ca-deficit nature of the protolith and the metasomatizing fluid. The co-existence of magnesite and hydromagnesite-hydrotalcite at the same outcrop is attributed to shifting pH of the metasomatizing fluid, percolation through the serpentinite and conductive cooling. Various factors, including reactant phase abundance and fluid nature likely influenced the final alteration mineralogy, providing insight into surface/near-surface transformations expected in CO₂ storage projects in peridotite terranes.

INTRODUCTION

¹ Corresponding Author: Mehmet Akbulut (makbulut@deu.edu.tr; mehmet.akbulut@deu.edu.tr)

Carbon dioxide is one of the most important components of the greenhouse gases (GHGs) contributing to the avalanching and dramatic outcomes of the climate crisis. The global concentration of atmospheric CO₂ has almost doubled since the dawn of the industrial age (from 280 ppm pre-industrial baseline to 407 ppm – data gathered in 2018) (cf. Blunden and Arndt, 2019; Snæbjörndóttir et al., 2020). Human activities are contributing increasingly to the global CO₂ input, making it increasingly challenging to attain the objective of limiting anthropogenic warming to 1.5-2 °C in accordance with the 2015 Paris Agreement (cf. Snæbjörndóttir et al., 2020 and the references therein), a legally binding international treaty for climate change counter actions that entered into force on 4th of November 2016 (cf. <https://unfccc.int/process-and-meetings/the-paris-agreement/the-paris-agreement>). Although there is now a much more common voice within the world policy makers on decreasing the CO₂ emissions in a shorter timespan than planned before, increasing severity of meteorological events (e.g., the scorching heatwaves, tropical cyclones etc.) reminds us that we need to scale up the efforts for reducing the global carbon footprint. However, reducing the carbon footprint is not an easy task. Several solutions and pathways have been suggested to reduce the huge anthropogenic contribution to the global carbon input. Mostly these cover long-term planning for reducing the future CO₂ emissions via shifting towards alternative energy resources instead of the currently extensively used conventional fossil fuels. Such actions however, bring another big problem: adjusting and providing sustainability of the global and national economic systems. Unfortunately, the level of atmospheric CO₂ has already reached alarming rates and needs urgent intervention with additional actions.

For this purpose, several improvised solutions have been inquired during the last three decades via observation of the nature's own remedies, such as the interaction between the biodiversity and geodiversity elements. Carbon capture and storage (CCS) is one of those mitigation strategies suggested for reducing the global impact of current (and potentially future projected) CO₂ emissions. CCS strategy focuses on removing and sequestering CO₂ directly from the air, aiming to negate the effects of the industrial age and includes a series of the CO₂ capture, separation, transportation and

storage process (cf. Snæbjörndóttir et al., 2020). Various methods suggested for this approach needs a clear understanding of the geological environment, resources, technological availability and application capacity of the operators.

Application of the CCS strategy starts with the CO₂ capture process. This may either be done at the point source that release the CO₂ to the atmosphere (e.g., fossil-fuelled power plants), or via direct air capture (DAC) technologies free from the point sources of emission. The second step is the CO₂ storage and it is directly related with the above-mentioned availability of the geodiversity elements. The captured and transported CO₂ needs to be stored in a certain potential geological host and in stable form. This host may be a certain hydrological (e.g., oceans) or a lithological element (e.g., saline aquifers, depleted oil/gas reservoirs, geothermal systems, unmineable coal seams, mafic or ultramafic reactive rocks, etc; cf. Aminu et al., 2017 and the references therein).

Among the several geological storage options, mineral carbonation stands in a different point due to its main reliance on mineral trapping mechanism. This process needs significant amount of reactive lithologies (mafic-ultramafic rocks), which may entrap the CO₂ in a stable form of carbonate phase (e.g., Lackner et al., 1995; Kelemen et al., 2011).

Understanding and utilizing mineral carbonation is especially important for a country like Türkiye that has a complex geological setting derived from the geodynamics of the Tethyan Oceanic Basin. Türkiye, lacking large oil and gas fields due its geological setting, naturally relies on coal for the fossil fuel items in its energy budget and has several active power plants (CPPs) for electricity production. Setting aside the small amount of land-accessed sedimentary basins for enhanced oil recovery (EOR), or potential brownfield or greenfield coal sites waiting to be evaluated as potential areas for enhanced coalbed methane recovery (ECBMR), Türkiye has an important amount of reactive mafic and ultramafic host assemblages suitable for mineral carbonation. More interestingly, nature already provides mineral carbonation analogues to reverse-engineer; the fully carbonatized and silicified serpentinites (listvenites). Listvenitic occurrences are described from the serpentinites and serpentinite-matrix mélanges worldwide, and northern and eastern ophiolites of Türkiye are

reported to have some significant examples of these (e.g., Legros, 1969; Yıldızeli et al., 1987; Leo et al., 1978; Ercan, 1982; Aydal, 1989; Genç et al., 1990; Larson and Erler, 1992; Erler and Larson, 1990; Tüysüz and Erler, 1993; Gültekin, 1993; Boztuğ et al., 1994; Koç and Kadioğlu, 1996; Uçurum, 1996; Reçber et al., 1997; Çiftçi, 1998; Uçurum and Larson, 1999; Oygür and Erler, 1999; Uçurum, 2000; Akbulut et al., 2006; Yavuz et al., 2022; Fig. 1). Although the initial focus of the listvenite studies had primarily been on their precious and base-metal contents, the mode of occurrences described in several earlier studies has invoked the curiosity of several scientists that seek pathways for a potential remedy for reducing the CO₂ levels (cf. Kelemen et al., 2020 and the references therein). In this study, we present a remarkable example of these natural mineral carbonation products hosted in the ophiolitic rocks of the Vezirler Mélange from the Kula (Manisa) region. To our knowledge, this is the first detailed study of these long-known alteration products of the region, in the aspect of understanding natural mineral carbonation mechanisms. With this attempt, we mainly hope to present a significant contribution to the growing literature on understanding and promoting engineered stable geological storage of CO₂ in mafic-ultramafic terranes.

GEOLOGICAL SETTING AND DESCRIPTION OF THE OUTCROP

Kula region is well known for its Quaternary volcanic extrusive outcrops. The significant geomorphology has let the region to be called as “Catacecau’mene” or “the burnt country” in the antiquity. Strabo defines these lands as black coloured plains of ashes and rocky mountains, having the looks of an internally burnt terrane that has later been quenched, correctly distinguishing the ashes or cinders from the hard rugged lava and describing the three cinder cones of the region (cf. Smith, 1854). This eye-catching volcano-stratigraphy has later been subject to many studies and lately resulted in the region to be established as an UNESCO Geopark (Kula-Salihli Geopark).

Kula region is located to the western termination of roughly east-west elongated northern ophiolitic belt of Türkiye (Fig. 1) and thanks to this geological setting, it includes many different geological assets, such as some notable hot springs and distinctive remnants of the Tethyan oceanic lithosphere.

The basement rocks in the Kula region are made of Pre-Mesozoic metamorphic rocks. These are overthrust by Mesozoic (Upper Cretaceous) Vezirler Mélange that consists of various lithologies such as serpentinized peridotites, radiolarites, cherty limestones, and mudstones (cf. Ercan, 1982). The ophiolitic series are unconformably overlain by Pliocene fluvial deposits accompanied by calc-alkaline volcanic extrusives and lacustrine deposits (cf. Ercan, 1982). Quaternary basaltic volcanites and alluvium overlay all of these lithologies. Tokçaer et al. (2005) indicates that the oldest episode of this volcanism is plateau basalts which include multiple main lava flows. The younger lava outflows have settled on the lower levels of the topography due to a topographic inversion resulting from the regional uplift after the initial volcanic episode (Hamilton and Strickland, 1841; Richardson-Bunbury, 1996; Tokçaer et al., 2005; Grützner et al., 2013). The second plateau basalts are formed by the lava flows that are produced by the youngest craters (cf. Tokçaer, 2000; Tokçaer et al., 2005). Among these lithologies described, some of the Vezirler Mélange outcrops in Kula region host some significant examples of hydrothermally induced silica-carbonate alteration described as listvenites (a.k.a. listwaenites). A general description of the silica-carbonate alteration products within the serpentinized peridotite outcrops of Vezirler Mélange were reported earlier by Ercan (1982). In that study, the protoliths of the serpentinized ultramafic rocks (serpentinites) in the mélange are interpreted to be harzburgite, dunite or lherzolite; and serpentinites are noted to host small magnesite and asbestos occurrences, possibly due to the introduction of CO₂-bearing water along their cracks and fissures. Ercan (1982) has also described a reddish, yellowish and brown coloured, silicified, carbonatized and limonitized crust overlying these ultramafic rocks and addressed this occurrence as “listvenite”.

A carbonatized and silicified serpentinite outcrop located west of Çakırca village is found juxtaposed next to the last phase of the Quaternary basaltic AA lava flows, just northeast of Kula (Figs. 2a and 2b). Although this roughly N60W elongated outcrop presents an alteration profile resembling to the above given earlier description, there are some significant field findings that need to be addressed. The alteration profile at the observed outcrop and surroundings includes an underlying friable and

mostly greenish-white coloured carbonatized and variably silicified serpentinite (CS-Srp), which can easily be distinguished in the field (Fig. 2b). Only very slightly carbonatized or non-carbonatized parts of the serpentinite retains the typical blackish green-green colour of serpentinite. Notably, carbonatization of the serpentinite is mainly represented by the occurrence of variably sized cauliflower-like and internally zoned carbonate nodules that reach up to 4 cm in size. These nodules coalesce to form irregularly distributed agglomerations (Figs. 3a-d). To a lesser extent, additional irregular carbonate veinlets also occur surrounding the relatively intact fragments of the friable serpentinites (Fig. 3d). Silicification of this lithology is macroscopically almost indistinctive and is limited to micro/nano silica polymorphs embedded within the carbonate nodules and accompanying silica varieties within the surrounding serpentine mesh matrix. The internally zoned carbonate nodules significantly and intensively gather and agglomerate towards the overlying iron-oxide stained silica-carbonate alteration crust (F_{sc}), resulting in the occurrence of a white coloured coalesced carbonate nodule zone (C_{nz}) located between the CS-Srp and the F_{sc} level (Figs. 2b and 3e-i). The C_{nz} shows of a variable thickness and irregular geometry.

In the field, the overlying iron-oxide stained silica-carbonate alteration crust (F_{sc}) resembles the typical appearance of a gossan zone. Its patchy distribution over the CS-Srp seems to mainly be related with the topographic inclination and slight mass movements, rather than intensive tectonic activity (Fig. 2b). There seems to be a very low angle (<10°) dipping towards NE along the F_{sc}-C_{nz} contact (Figs. 3e-h). The F_{sc} is generally highly competent with respect to the underlying C_{nz} and the CS-Srp. Its macroscopic appearance is somewhat inhomogeneous (Fig. 3i). Most parts of this crust show reddish brown coloured chalcedonic appearance with ubiquitous greenish-black to green coloured chalcedony-like blotches that can be determined in hand specimens. Hammering these parts of the crust usually releases the characteristic burnt flint-like odour that is typical for the silicified formations. However also there are some parts that are duller, yellowish brown coloured and less resistant. Some rare parts of this crust are also heavily limonitized and show a typical yellow ochre

colour. The Fsc is irregularly crosscut by late stage stockwork veinlets, which further evolve into boxwork structures (sample 18B in Fig. 3i).

SAMPLING AND ANALYTICAL METHODS

A total of 20 samples were collected from the carbonatized and silicified serpentinites (CS-Srp), coalesced carbonate nodule zone (Cnz) and the overlying iron-oxide stained silica-carbonate alteration crust (Fsc). Doubly polished thin sections (24x46 mm) were prepared at the sample preparation facilities of Geological Engineering Department of Dokuz Eylül University (DEU, Izmir, Turkey) for petrography, X-ray diffraction and Laser-Raman spectroscopy studies. The thin sections were studied for initial determination of the rock-forming and opaque minerals and their textures under polarizing and reflected light using a Leica DM2500P microscope at the Department of Geological Engineering of DEU. The initial petrographic characterization was supported by energy-dispersive X-ray spectroscopy (EDS) and back-scattered electron (BSE) images, where areas of interest on the thin sections were studied using a Scanning Electron Microscope (model: FEI Quanta 250 FEG SEM) installed at the IzTech Integrated Research Centers of Izmir Institute of Technology (IzTech IRC, Izmir). No coating was applied on the thin sections. Further in-situ characterization was made by Laser-Raman spectroscopy at the Central Research Laboratory of İzmir Katip Çelebi University (IKCU CRL, Izmir) using a Confocal Renishaw inVia Raman Microscope and Spectrometer. All the spectra from Laser-Raman spectroscopy were obtained under 20x to 100x optical zoom, using 532 nm excitation and 2400 line/mm grating settings. Cosmic-Ray Event (CRE) related peak and background removal was performed using CrystalSleuth Raman Spectroscopy software (Laetsch and Downs, 2006). The acquired spectra were evaluated in comparison with RRUFF Raman spectral library (<http://rruff.info>). Additional qualitative mineralogical characterization was obtained from pulverized and random oriented whole-rock and mineral separates using a Rigaku MiniFlex 600 X-Ray Diffractometer (XRD) installed at the X-Ray Laboratory of DEU Department of Geological Engineering. The measurements were completed using CuK_α radiation

($\lambda=1.54059 \text{ \AA}$) and Ni filter over the 2θ range of $4-65^\circ$ with a $2^\circ/\text{m}$ scan speed. The voltage was set to 33 kV and the current to 15 mA during the analytical runs. The crystalline phases were identified via using the PDXL2 software package (Rigaku).

MINERALOGICAL AND TEXTURAL FINDINGS

FROM THE ALTERATION PROFILE

The very slightly carbonatized or non-carbonatized serpentinite is generally blackish-green to green coloured and dominantly made of serpentine minerals. Both pseudomorphic and non-pseudomorphic serpentine textures are present and form the typical mesh texture (Fig. 4a). No relict olivine is detected. Although the types of serpentine minerals are not strictly differentiated, the abundance of the net-like patterns and fibrous cross-cutting veinlets suggests a dominance of lizardite and chrysotile over antigorite. A significant number of bastite transformations and relict orthopyroxenes are found (Fig. 4b). The serpentinite paragenesis also includes euhedral, subhedral and anhedral garnets within and/or at the borders of the bastites and/or relict orthopyroxenes (Figs. 4b-f). They can be optically distinguished via their isotropic appearance and higher relief with respect to the surrounding phases. Raman spectrum of these garnets present three distinct spectral regions with relatively strong, high intensity bands around $353-370 \text{ cm}^{-1}$, $493-516 \text{ cm}^{-1}$ and $817-875 \text{ cm}^{-1}$ and is in very good agreement with Raman spectral data of the andradite in the literature (see Supplementary Fig. 1S; cf. Hofmeister and Chopelas, 1991; Štubňa et al., 2019). The qualitative chemical composition obtained via electron dispersive spectrometry (EDS) also supports this determination (see Supplementary Fig. 1S). The andradites at the contacts with orthopyroxene and serpentine are partially replaced by dolomite and hematite (hematite-I), whilst the ones embedded inside the orthopyroxene relicts seems relatively unaltered and show only minor hematite replacements (Figs. 4b-f). In some parts of the serpentine mesh matrix, there are peculiar leftover voids encircled by dolomite coronas (Figs. 5a-d). The outlines of the voids remind the geometry of a cubic phase. EDS spectrum of a rarely found intact grain encircled by dolomite suggests pre-existence of a calcium and magnesium bearing cubic silicate phase,

probably a garnet variety, within those voids (Fig. 5d and Supplementary Fig. 2S). Presence of significant bastite relicts after orthopyroxene and minor remnants of andradite in the paragenesis indicates a mantle protolith bearing minor amounts of clinopyroxenes such as dunite or harzburgite. Relict anhedral chromite grains are replaced by ferrite-chromite and magnetite (magnetite-I) which are further replaced by hematite (hematite-II) and goethite along the grain boundaries and cracks (Figs. 6a and 6b). There are also discrete subhedral/anhedral magnetite occurrences (magnetite-II) that are replaced by hematite-II (Figs. 6c and d).

Intensive carbonatization of the serpentinites are mainly represented by the presence of variably sized and mainly carbonate bearing cauliflower-like nodules (Figs. 3a-c) and minor carbonate veinlets (Fig. 3d) within the altered (greenish-white coloured and partially silicified) serpentine in the lower part of the alteration profile (Fig. 3i). The randomly distributed nodules show a tendency to cluster along certain discontinuity planes in the serpentinite mélange. The carbonate dominated nodules located outwards the contact with the Fsc, towards the lower parts of the CS-Srp outcrop, are mainly made of fine-grained cores and coarser-grained rims (sample N1 in Fig 3i). Under polarized light and crossed polars, the fine-grained inner parts (cores) look darker in colour (see Supplementary Fig. 3S). The outer parts (rims) contrarily present high order interference colours and an acicular morphology, which is much more distinctive in the back-scattered electron images (see Supplementary Fig. 3S). The EDS spectra collected from the core and rim phases respectively shows similar elemental abundances of C (31.18 and 28.55 wt. %), O (48.22 and 49.86 wt. %), Mg (18.08 and 17.56 wt. %), Si (1.87 and 2.71 wt. %), Na (0.29 and 0.28 wt. %) and Cl (0.24 and 0.41 wt. %) (see Supplementary Fig. 3S). There is a very subtle Al (0.05 wt. %) and Ca (0.09 wt. %) presence in the core, and Fe presence (0.63 wt. %) in the rim (see Supplementary Fig. 3S). The Si content in the EDS spectra suggests presence of silica (nano?) particles in the areas selected for EDS analysis. The whole-rock XRD patterns from the discrete carbonate nodules present peaks of hydromagnesite $[\text{Mg}_5(\text{CO}_3)_4(\text{OH})_2 \cdot 4\text{H}_2\text{O}]$, serpentinite (lizardite?) and hydrotalcite $[\text{Mg}_6\text{Al}_2(\text{OH})_{16}[\text{CO}_3] \cdot 4\text{H}_2\text{O}]$ (see Supplementary Fig. 3S).

Conversely, the nodules sampled from and in the immediate vicinity below the Cnz (Samples 2, 3, 5, 8 and 9 in Fig. 3i) are mainly made of magnesite varieties that show a ubiquitous textural zoning from core to rim (Figs. 7a-h). In general, the zoning starts with a fine-grained magnesite (Mgs-I) at the core, and continue outwards with coarse grained and comb-textured magnesite (Mgs-IIa) in both the irregularly distributed carbonate nodules within the serpentinite mesh matrix (Fig. 7a) and their coalesced counterparts that comprise the Cnz (Figs. 7b-c). A variance of this two-stage zoning encountered in a sample from the Cnz presents magnesite nodule remnants enveloped by iron-oxide (goethite-limonite) layers and later stage magnesites (sample 5 in Fig. 3i, Fig. 7d). On the other hand, additional three zones can further be determined from the irregularly distributed magnesite dominant nodules (Figs. 7e-g). The first of the additional zones is a fine-grained lattice-bladed (almost lepisphere-like) magnesite (Mgs-IIIa) zone (Fig. 7h). This additional zone is surrounded by recurrent coarse-grained and comb textured magnesite (Mgs-IIb) layer and another fine-grained lattice-bladed magnesite (Mgs-IIIb) layer outwards (Fig. 7h).

The elemental distribution of the magnesite zoning obtained by the EDS spectra illustrates that the variance of the major components C, O, Mg and Si in the fine-grained magnesite (Mgs-I) at the core and the surrounding coarse-grained and comb-textured magnesite (Mgs-IIa) is almost insignificant (Figs. 9a and 9b). This is a notable resemblance with the almost homogenous elemental abundances encountered in the hydromagnesite nodules with fine-grained cores and coarse-grained rims (see Supplementary Fig. 3S). The Si abundance in the EDS spectra again indicates the presence of silica (nano?) particles in the areas of interest. However, there is also a distinct Mg and Si fluctuation along the additional Mgs-IIIa, Mgs-IIb and Mgs-IIIb layers. The Mg and Si abundances shows an exactly opposite behaviour along the recurrent layers; Mg decreases with the increasing Si content and vice versa (Fig. 8b). This fluctuation is also traceable in the Raman spectra from the fine-grained cores and coarse-grained surrounding layers in both the stacked nodules in Cnz and randomly distributed nodules in the CS-Srp. In general, the Raman spectra of the fine-grained core zones and the coarse-grained surrounding zones are significantly conformable with the magnesite spectra from the

literature (Figs. 9c and 9d). However, Raman spectra of the lattice-bladed magnesite layers including higher Si contents shows a composite spectrum at the analysed areas revealing coexistence of magnesite (peaks around 213, 330, 739 and 1094 cm^{-1}) and opal-CT (typical broad bands around 300-350, and peaks around 781 and 1075 cm^{-1}), a variant of opal made of disordered α -cristobalite and α -tridymite (cf. Wilson, 2014 and the references therein) (Fig. 8e).

The uppermost zone of the alteration profile, the iron-oxide stained silica-carbonate alteration crust (F_{sc}, Figs. 3e-i, also see samples 1, 4, 7 and 18B in Fig. 3i), is characterized by an alteration mineralogy made of carbonate nodules and veinlets, micro- to cryptocrystalline silica infills and veinlets, and abundant secondary iron oxides (mainly in the form of goethite-limonite, hematite-II and ubiquitous iron-staining). These phases occur over the prior serpentinite mineralogy composed of serpentine minerals and euhedral to subhedral chromites. Relict patches of iron-oxide stained serpentinite mesh texture can occasionally be determined (Fig. 9a). The overall paragenesis of F_{sc} resembles to that of the greenish-white coloured carbonatized and silicified serpentinites (CS-Srp) described from the base of the outcrop, however the iron-oxide and silica abundance here creates a macroscopic difference.

The carbonate nodules are present at the lower part of the F_{sc} near the contact with the C_{nz} (alteration profile given in Figs. 3i, microphotograph given in Fig. 9b). These carbonate nodules are embedded within an iron-oxide stained serpentine mesh matrix including relict chromite grains and they are accompanied by coarser grained carbonate veinlets (Fig. 9b). The carbonate nodules seem to show a fine-grained core and coarse-grained grain rim, a zoning pattern similar to the ones observed in the C_{nz} counterparts located below. Moreover, they similarly coalesce to form larger carbonate agglomerations. The whole-rock X-Ray spectrum obtained from the samples from the lower part of the F_{sc} reveals coexistence of magnesite, dolomite and minor amorphous phases (see Supplementary Fig. 4S), indicating presence of two different types of carbonates (possibly as magnesite nodules and dolomite veinlets) at the lower part of the F_{sc}. Conversely, carbonatization in the upper part of the F_{sc} is mainly represented by carbonate and silica veinlets cross-cutting the relict serpentinite mesh

patches (Figs. 9c-e). Carbonates within these veinlets, which are contemporaneous with or postdating the silica precipitation, are determined as dolomite via X-Ray diffraction (see Supplementary Fig. 4S). Silica varieties found within these parts are generally in the form of late stage radial to spherulitic micro- to cryptocrystalline silica (Opal-CT?) infills and veinlets. The relict chromites of the original serpentinites are generally found to be replaced by hematite-II along their rims, probably as latter occurrences after the prior magnetite-I replacement of the chromite (Figs. 9f and 9g). Hematite-II is also found as discrete or arrayed small neocrystals, possibly as a total replacement product from the magnetite-II grains previously formed during the serpentinization (Figs. 9f and 9h).

NATURE OF THE GEOTHERMAL FLUIDS

Tokçar (2000) has compiled and analysed several water samples from the study area. Here, we present data from seven samples of this dataset. Four of these water samples have temperatures ranging from 33 to 55 °C and are classified as geothermal waters (GW). A water sample with an electrical conductivity of 3380 $\mu\text{S}/\text{cm}$ and temperature of 16.8 °C is classified as mineral water (MW). Other water samples with temperatures varying between 11.9 and 12.2 are classified as cold waters (CW). Data collected from these waters are presented in Table 1.

The compiled waters are considered based on their major ion concentrations (c_i in $\text{meq}\cdot\text{L}^{-1}$), where $c_i > 25\%$ of the C_{total} (total concentrations in $\text{meq}\cdot\text{L}^{-1}$) defines the water facies. Na and Mg are the dominant cations in the geothermal waters as they correspond to over 85% of C_{total} , whereas Ca and K constitute smaller than 15% of C_{total} . For anions, HCO_3^- is dominant (c_i between 2851 to 3122 $\text{mg}\cdot\text{L}^{-1}$) and corresponds to more than 86% of C_{total} . Cl concentrations range from 154 to 201 $\text{mg}\cdot\text{L}^{-1}$, making it the second most abundant anion, constituting the 9% of total concentration in $\text{meq}\cdot\text{L}^{-1}$. According to these results, the predominant geothermal water (GW) type is Na- HCO_3^- -Cl. The predominant cations in the cold waters (CW) are Ca, Na and Mg. HCO_3^- and Cl are the predominant anions. All of the geothermal waters (GW) and the mineral water (MW) sampled from the study area

and surroundings present total inorganic carbon contents (TIC as CO₂) between 2205-2507 mg/l (Table 1).

DISCUSSION

Tectonic and Lithological Controls and the Fluid Geochemistry

Most of the bulk natural carbonate occurrences in the geological environments take place in certain lacustrine/marine sedimentary realms. These mainly occur via chemical sedimentation processes and lead to the formation of various types of sedimentary calcareous lithologies (e.g., limestones, dolostones, marls, etc.). However, significant amounts of carbonate minerals can also form in magmatic or metasomatic/hydrothermal environments. The formation of carbonate minerals in the metasomatic/hydrothermal environment is an epigenetic alteration phenomenon and requires the introduction of CO₂-rich fluids into reactive host lithologies leading to the carbonatization of the original lithologies. The reactivity of the original host is mainly linked to its mineralogy and the degree of deformation. In this aspect, the peridotites are one of the most suitable reactive hosts.

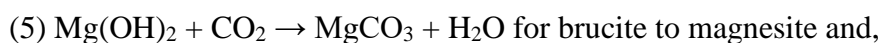
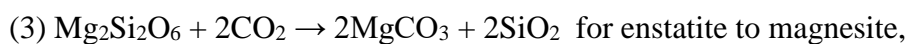
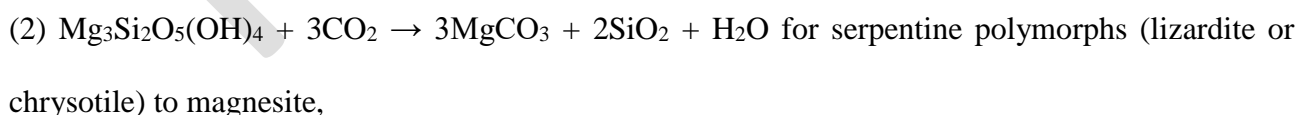
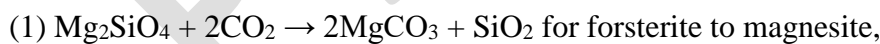
Carbonatization of peridotites appears as three main forms: (1) carbonate (generally magnesite) veins within serpentinized peridotites, (2) as carbonate deposits around springs in peridotite catchments, and (3) as totally carbonatized and silicified metasomatic bodies within serpentinized peridotites, commonly addressed as listvenites (cf. Kelemen et al., 2011). Regardless of the type of the carbonate, all of these occurrences need a main conduit for the introduction of the CO₂-laden fluids to the system for occurrence of this kind of alteration and/or precipitation-deposition. Hence, understanding of the process needs determination of both tectonic and lithological controls.

The original orientation of the lower carbonatized and silicified serpentinite (CS-Srp), the overlying coalesced carbonate nodule zone (Cnz) and the upper iron-oxide stained silica-carbonate alteration crust (Fscc) of the alteration profile addressed in this study seems to be somewhat displaced/dislocated at the outcrop scale. This is largely due to the different rheological behaviour of

the units which have resulted slight mass movements. However, there is a laterally traceable main N60W strike and a very low angle NE dipping trend ($<10^\circ$) (Figs. 2 and 3f and 3h). This suggests a NW elongated and NE dipping main discontinuity zone for the main tectonic control for influx of CO₂-bearing geothermal fluids.

The carbonatization and silicification in the studied outcrop is also lithologically controlled by the heavily serpentinized peridotite host. The main reactive phases to be dissolved by the CO₂-rich fluid influx to form carbonate species in peridotites are the minerals olivine, serpentine and brucite. Olivine by itself has a significant potential to produce sufficient alkalinity for carbonatization. However, as serpentinization of peridotites takes place, the primary olivines and orthopyroxenes of the peridotite hydrolyse to transform mainly into the serpentine group minerals producing minor accompanying opaque oxides or alloys (e.g, magnetite, Ni-Fe alloys), silicates (e.g., talc, tremolite/actinolite, chlorite) or hydroxides (e.g., brucite) according to the P-T parameters (cf. Holm et al., 2015). This process also converts the rock's original coarse-grained and interlocking magmatic, recrystallization and/or mantle deformation (protogranular to porphyroclastic) textures into a much finer-grained and more permeable alteration texture (serpentinite mesh texture) that may further facilitate interaction of secondary CO₂-rich fluids with the phases. The close spatial correlation of listvenites with heavily serpentinized peridotite and serpentinite matrix *mélange* hosts around the world confirms this.

In several earlier works, some idealized reactions are considered for the carbonatization of serpentinite with the introduction of CO₂ component such as (cf. Kelemen et al., 2020):



(6) $2\text{Mg}(\text{OH})_2 + \text{Mg}_3\text{Si}_2\text{O}_5(\text{OH})_4 + 4\text{CO}_2 + \text{H}_2\text{O} \rightarrow \text{Mg}_5(\text{CO}_3)_4(\text{OH})_2 \cdot 4\text{H}_2\text{O} + 2\text{SiO}_2$ for coexisting brucite and serpentine polymorphs to hydromagnesite.

Reactions (1) to (5) shows that the desilication of Mg-silicates during carbonatization of a peridotite and/or serpentinite should produce silica along with magnesite and/or dolomite. A Mg-hydroxide parent phase such as brucite on the contrary, does not require occurrence of such an additional product. Additionally, the presence of Ca in the reactants would produce dolomite and/or similar Ca-bearing carbonates rather than the magnesite. Metastable hydrated Mg-carbonates such as hydromagnesite may also accompany these products (reaction 6).

The paragenesis described from the alteration profile in the study area indicates a magnesite/hydromagnesite dominant carbonatization accompanied by micro- to cryptocrystalline silica (Opal-CT). Only very small presence of dolomite is reported either as coronas surrounding the primary andradites in the very slightly carbonatized blackish-green to green coloured sample from CS-Srp, or as dolomitic components in the silica-carbonate veinlets in the Fsc. The serpentine group minerals are the main Mg bearing phases in the host serpentinites; no brucite is detected in the studied thin sections and the powder diffraction data.

Minor presence of dolomite in the very slightly carbonatized serpentinite indicates limited presence of Ca-bearing primary phases in the protolith and of dissolved Ca-bearing species in the metasomatizing fluids. Although occasional bastites after enstatite porphyroclast remnants are found, no diopsidic pyroxene could be described from the samples. Hence, the primary presence of clinopyroxenes can only be attributed to the exsolution lamellae in the orthopyroxene porphyroclasts, if there were any. Other than that, the only directly observed Ca-source phase in the serpentinite is andradite surrounded by dolomite coronas. The significant dominance of Mg-dominant carbonates over the Ca-bearing ones shows a severe Ca deficiency in the system during the carbonatization of the peridotites.

It is recently reported that presence of magnesite-quartz assemblage requires fluid CO_2 concentrations of ~2,500 ppm at 100 °C and 5 kbar (Beinlich et al., 2020 and the references therein). The TIC

contents (as CO₂) of the recent geothermal and mineral waters in and around the study area, and the mineralogy of the carbonatized and silicified alteration rocks shows a good agreement in this aspect. Hence, similar to the sampled recent Na-HCO₃⁻-Cl type geothermal waters from the study area, the fluid that had been responsible for the carbonatization of the peridotites should have also been a Ca-deficit solution.

Additionally, the magnesite/hydromagnesite are ubiquitously found as recurrently zoned nodules within a silicified matrix that partly preserve relict original serpentinite mesh texture. Regarding this, it is suggested that the repetitive Si-rich and Si-poor magnesite zones in the magnesite nodules might be helpful in deciphering the reactants of the phase transformations during progressive carbonatization. The analysed areas in the fine-grained magnesites (Mgs-I) at the central parts of the magnesite nodules generally present low Si content and show almost typical magnesite Raman spectra (Fig. 8). Hence, one may speculate that replacement of Mg-bearing non-silicate phases such as brucite (see reaction 5) could be much more dominant than the desilication of serpentine at the initial stages of carbonatization for the formation of these magnesites. At low temperatures, dissolution of brucite in water is reported to be faster than olivine and chrysotile by four orders of magnitude (Beinlich and Austrheim, 2012; Mumpton and Thompson, 1966; Pokrovsky and Schott, 2004; Snow and Dick, 1995; Boschi et al., 2017). Hence, when brucite is present in the serpentinite paragenesis, it is described as the first phase to be replaced during carbonatization, either by magnesite (at T > 100 °C) or Mg-hydroxycarbonate species (at T < 80–60 °C) (Klein and Garrido, 2011; Hopkinson et al., 2012; Gautier et al., 2014; Boschi et al., 2017).

However, as indicated earlier, brucite has not been encountered in the studied samples. This may be related to our sampling pattern or overlooking which might have resulted in a failure to recognize a possible protolith heterogeneity within the outcrop (i.e., coexisting brucite-bearing and brucite-free serpentinites). Serpentinite paragenesis is considered to be related with the protolith mineralogy, chemistry of the influxing fluid, or the temperature (Boschi et al., 2017 and the references therein) and the protolith mineralogy might have had an important influence for the studied outcrop in Kula.

Here, the sampled carbonatized and silicified serpentinites (CS-Srp) are found to include no bastites (pyroxene relicts). In line with this, the bastite-bearing very slightly carbonatized serpentinite also has shown no significant carbonatization other than minor dolomite coronas around andradite.

The lack of brucite may additionally be partially related to the local presence of andradite due to the heterogeneity of the protolith. We believe that the origin of these reported andradite garnet in the serpentinite host has a metamorphic origin rather than a high-pressure history as they show no kelyphitic rims which are ubiquitous for their counterparts in garnet peridotites. Andradite stability is highly sensitive to silica activity and in serpentinites where native iron is dissolved into Fe-Ni alloys (e.g., awaruite), andradite may form in the expense of magnetite and diopside \pm brucite of the initial paragenesis (Frost and Beard, 2007). Hence, such a pre-carbonatization process, potentially accompanied by elevated oxygen fugacity, might have also taken a role for the decrease in the modal amount of brucite, facilitating its total consumption in favour of magnesite during carbonatization.

Regarding the carbonatization represented by the recurrently zoned magnesite nodules in the possibly previously brucite-bearing serpentinite part of the protolith, we may suggest formation of the initial magnesites in expense of brucite rather than serpentine polymorphs. The second and fourth magnesite zones outwards (Mgs-IIa, Mgs-IIb; Fig. 8) also present resembling elemental and Raman spectra. The only different observation between these zones may be slower reaction rates which is hinted by the coarser grain sizes. In contrast, the analysed areas at the third and fifth magnesite zones outwards (Mgs-IIIa, Mgs-IIIb; Fig. 8) show distinctly higher Si contents and a composite Raman spectrum including both magnesite and opal-CT peaks. They are also significantly different with their lattice-bladed (lepisphere-like) morphology. These findings indicate increased presence of silica (nano?) particles in the areas/points of interest, and imply the increased dominance of serpentine desilication over brucite replacement for the formation of these lattice-bladed silica-bearing carbonates. Thus, the repetitive zoned structure of the nodules may be related with the change of reactant phases (brucite and serpentinite polymorphs) due to the shifting relative abundances during the progressing alteration. On the other hand, the composite Raman spectrum from these Si-rich magnesite zones (Fig. 8e) may

also be attributed to episodically attained silica oversaturation during alteration. Silica activity is also controlled by other parameters such as the temperature, X_{CO_2} and Si content of the fluid, reactive surface area within the protolith, or the water/rock ratio during the fluid influx. Thus, intermittent replenishment and/or cooling of the carbonatizing fluid, its shifting physiochemical conditions, or influx rate should also be considered in the formation of such a recurrently zoned structure.

Although the topmost part of the alteration profile, entitled the iron-oxide stained silica-carbonate alteration crust (Fsc), mineralogically resembles to the below standing carbonatized and silicified serpentinite (CS-Srp), it diverges with its iron-oxide abundance, additional stage silica-carbonate veinlets and remarkably much more resistant morphology. These notable features and the spatially consistent presence of the Fsc over the CS-Srp suggest that the Fsc may be a product of combined CO_2 driven alteration and supplementary surficial weathering processes near the paleo-surface. The iron oxide enrichment of the topmost part of the alteration zone might have taken place earlier and/or concomitantly with the interaction of CO_2 -laden fluids that trigger the main carbonatization of the host serpentinite.

Implications from the Mg-hydroxycarbonate Occurrences

Magnesite is identified as the dominant stable carbonate phase in the silica-carbonate alteration products of the Vezirler Mélange around Kula. It occurs as discrete or agglomerated nodules, mainly at the lower parts of the iron-oxide stained silica-carbonate alteration crust (Fsc), form the coalesced carbonate nodule zone (Cnz) of the alteration profile, and occur at the immediate upper part of the carbonatized and silicified serpentinite (CS-Srp) just below the Cnz. Dolomite is another stable carbonate species found in the alteration profile and occurs as reaction coronas around minor amounts of Ca-bearing parent phases in the CS-Srp or as accompanying phases within the microcrystalline silica bearing stockwork veinlets in the Fsc. Magnesite and dolomite are almost ubiquitously found carbonate species in the fully carbonatized-silicified peridotites (a.k.a. listvenites). However,

presence of Mg-hydroxycarbonate nodules at the lower to middle segments of CS-Srp, in the form of hydromagnesite-hydrotalcite (hydromagnesite prevailing), is a notable finding to be addressed.

Mineral carbonation in the ultramafic rocks can form during serpentinization, post-serpentinization hydrothermal carbonatization, or weathering which is partially also being controlled by microbial activity (cf. Power et al., 2013). While the formation of anhydrous magnesium carbonates takes place hydrothermally as veins or discretely formed microcrystalline grains within the silica-carbonate altered peridotite, the metastable hydrous magnesium carbonate species are usually reported to occur as authigenic precipitates or chemical weathering products in alkaline springs and playas (e.g., spring deposits in the Semail ophiolite – e.g., Giampouras et al., 2020; Scheller et al., 2021, and hydromagnesite-magnesite playas such as Salda Lake in Türkiye - cf. Braithwaite and Zedef, 1996; Zedef et al., 2000; Balci et al., 2020, and Atlin playas in Canada - Power et al., 2009; 2014). In near-surface environments, precipitation of stable magnesite species is inhibited by the strong hydration shells surrounding aqueous Mg^{2+} ions, and this results in formation of hydrated magnesium carbonate minerals instead of the magnesite (e.g. Königsberger et al. 1999; Power et al., 2013). The occurrence of magnesite at room temperature is almost impossible, and it is mostly preceded by a hydrated precursor at higher temperatures (60–120 °C) (Boschi et al., 2009). On the other hand, reaction of brucite $[Mg(OH)_2]$ with CO_2 can also produce various metastable Mg-hydroxycarbonates (e.g., hydromagnesite- $[Mg_5(CO_3)_4(OH)_2 \cdot 4H_2O]$) which eventually expected to mature into the most thermodynamically stable phase, magnesite ($MgCO_3$) (Zhang et al., 2000). An example for the formation of hydromagnesite after brucite is given in the work by Mumpton and Thompson (1966), where the absence of iron-rich brucite $[(Mg_{10}Fe_2)(OH)_{24}]$ is reported in favour of pyroaurite $[Mg_6Fe_2CO_3(OH)_{16} \cdot 4H_2O]$ and coalingite $[Mg_{10}Fe_2CO_3(OH)_{24} \cdot 2H_2O]$ of hydrotalcite supergroup at the surface weathering zone. Mumpton and Thompson (1966) further indicate presence of hydromagnesite veinlets and artinite $[Mg_2(CO_3)(OH)_2 \cdot 3H_2O]$ coatings on the surfaces of the serpentinite blocks they studied, and mention local concentrations of pea-sized concretions of dominantly hydromagnesite in the greenish white asbestos matrix. Mumpton and Thompson (1966)

interpret these latter occurrences as break-down products of iron-rich brucite in the presence of excess ground waters which leave behind a residue of amorphous iron oxides. Same transformations are also suggested by Hostetler et al. (1966). Hence, the variety of hydromagnesite formation pathways makes understanding the nature of hydromagnesites essential for revealing the details of the carbonatization process(es) in the Vezirler Mélange around Kula.

A similar occurrence has been described by Stamatakis and Mitsis (2013) in an earlier study from the serpentinized peridotites the Sousaki-Geraneia and Kaloni-Methana areas in the southeastern termination of the internal Hellenides in mainland Greece. In their study, Stamatakis and Mitsis (2013) have reported presence of Mg-rich hydroxycarbonates (hydromagnesite and pyroaurite) along with huntite $[\text{CaMg}_3(\text{CO}_3)_4]$, and magnesites in form of white nodules, fissure fillings-crusts and veins in highly weathered/altered ultrabasic rocks that locally appear as greenish or yellowish-brown coloured earthy matrix. Stamatakis and Mitsis (2013) describe the hydromagnesite occurrences in form of cotton balls and fissure fillings within highly altered serpentinites, and the magnesite occurrences as white nodular/cauliflower shaped accumulation layers. These researchers further describe cauliflower or lettuce-leave shaped hard magnesite assemblages near the present-day surfaces, located above the hydromagnesite accumulations. At first glance, a similarity between these descriptions and the observations from the alteration profile in Kula, particularly in the spatial and mineralogical aspects, is remarkable.

Brucite is one of the prime candidates for the formation of magnesite at depth, however at near-surface and/or hydrous surface environment, it is preferentially converted to Mg-hydroxycarbonates; to hydromagnesite under at least 10^{-6} atm CO_2 partial pressure (P_{CO_2}), and to pyroaurite, artinite and/or coalingite at even smaller P_{CO_2} values (Hostetler, 1960; Hostetler et al., 1966). Hence, the presence of hydrotalcite peaks accompanying the hydromagnesite in the XRD-spectrum of the nodules (Fig.7) may indicate smaller ($<10^{-6}$ atm) P_{CO_2} values for the formation of Mg-hydroxycarbonates in Kula region.

Moreover, hydromagnesite to magnesite transformation has a negative ΔG_r value (-31.86), indicating the reaction tendency to move towards the products end and indicating that magnesite should be the final stable species. This, and the overlying position of the nodular magnesites above the hydromagnesite-hydrotalcite nodules, as discrete grains at the upper part of CR-Srp, agglomerated (coalesced) grains at the Cnz, and again discrete grains at the lower part of Fsc, may imply dehydration of hydrated carbonate precursors (in this case the hydromagnesite-hydrotalcite) at the uppermost parts of the weathering profile. However, such an approach would need an explanation on why all of the carbonate species have not been dehydrated all along the outcrop.

On the other hand, formation of hydromagnesite under moderately low Mg activities requires strongly alkaline conditions. This is also possible under weaker alkaline conditions if the Mg activity is higher (Fig. 10). Thus, the co-existence of magnesite and hydromagnesite-hydrotalcite at the same outcrop may alternatively be explained by the shifting of pH of the CO₂-rich fluids during influx and conductive cooling. It may be suggested that the pH of the initially introduced low pH CO₂-bearing fluid has resulted in an intense water/rock interaction dissolving Mg source species such as brucite or serpentine polymorphs increasing Mg and additionally Si concentrations in the presence of the latter. The environment should have been started to be buffered during this process as the fluid influx should also have been partially depressurized along the permeable tectonic discontinuity due to the loss of CO₂. This would lead to further increase of the pH to almost neutral values facilitating the precipitation of Mg-carbonates (magnesite for $T > 80$ °C). Subsequently, the fluid influx should have been percolated through the serpentinite host and has to be further cooled during this infiltration. Such a conductive cooling process could lead to formation of lower temperature hydrated Mg-carbonate species outwards (i.e., hydromagnesite-hydrotalcite) rather than the magnesite counterparts within and in the immediate vicinity of the main fluid channel (the low angle discontinuity zone between CS-Srp and Fsc). The presence of amorphous silica in the CS-Serp zone below and the Fsc zone above the main fluid channel is also in good agreement with the temperature decrease and therefore decreasing Si solubility during progressing alteration. As mentioned earlier, a combination

of several factors such as the relative abundance of the reactant phases, nature and replenishment rate of the fluid and changes in the water/rock ratio should have also been effective in the final alteration mineralogy.

CONCLUSIONS

Ultramafic rocks are considered as possible targets for mineral carbonation, one of the mitigation strategies pronounced as remedies for the climate crisis taking its toll today. Geological carbonatization products found in nature (listvenites) illustrate the potential analogical approach for the solution. Peridotites have substantially higher carbonation potential than that of the basalts; ideally total carbonation of the peridotites (listvenites) presenting a final reaction assemblage comprising mainly magnesite and quartz (Oelkers and Gislason, 2023).

This current report on the alteration products of the Vezirler Mélange around Kula shows significant aspects of the mineralogical transformations expected to take place in a serpentinite paleo-surface and the shallow weathering zone beneath. Our field and mineralogical studies remarks the controls of the lithology, tectonics, and initial and later shifted fluid chemistry/ physicochemical conditions on the formation of the carbonate species during carbonatization of the peridotites. These controls have been effective in the formation of the bottom to top alteration profile that is made of carbonatized and silicified serpentinite (CS-Srp), coalesced carbonate nodule zone (Cnz), and iron-oxide stained silica-carbonate alteration crust (Fsc).

Concurring with the earlier works (e.g., Boschi et al., 2017), the role of the lithological heterogeneity looks especially significant. The pyroxene-bearing and pyroxene-free peridotite protoliths, and presence and modal amounts of their serpentinitization products (e.g., brucite, andradite, serpentine polymorphs etc.) seem to be one of the controlling factors for intensity of the carbonatization. Shifting relative modal abundance of the reactant phases, physicochemical properties and replenishment rate of the fluid, and changes in the water/rock ratio in the prograding carbonatization should have also been effective in the final alteration mineralogy.

The low angle tectonic discontinuity zone, which has been marked by the presence of the coalesced carbonate nodule zone (Cnz), has acted as the feeder conduit for the CO₂-rich fluid influx. The initial low pH CO₂-bearing fluid flux should have dissolved Mg source species (e.g., brucite or serpentine polymorphs) and increased Mg and Si concentrations. Partial depressurization, related to the loss of CO₂ along the permeable tectonic discontinuity, should have buffered the environment to almost neutral pH values and triggered the precipitation of Mg-carbonates (magnesite) along and in the vicinity of the conduit. The precipitation of the hydrated Mg-carbonate counterparts (hydromagnesite-hydrotalcite) outwards the discontinuity zone should have been related with the percolation and conductive cooling of the fluid.

Overall, the data presented here presents a good analogy on surface/near-surface transformations that may take place at shallow levels of potential host rocks for future projects making use of either underground injection methods and/or artificial pit-lakes (or tailing ponds) of abandoned open-pit mines. The detailed description of the reactant species should be followed by investigation of other factors on fluid-rock interaction during carbonatization for further work. A detailed understanding of the total paragenetic assemblage, rock tonnage to be subjected to the carbonatization process, fracture-controlled permeability of these host rocks, geochemistry of the fluids involved, reaction rate, and possible risks of reaction passivation should be addressed on site basis. Such efforts would help accelerate settling the scientific basis for the engineered CO₂ storage in peridotites.

As a final note, the carbonatization example presented in this study also has another unique value due to its incorporation as a geosite within the UNESCO Kula-Salihli Geopark. This study we believe, by addressing a significant natural occurrence on an already described geosite, will also contribute to increase the situational awareness and understanding on potential sustainable remedies on global climate crisis.

ACKNOWLEDGEMENTS

We would like to express our gratitude to the two anonymous reviewers and the editor Dr. José Alberto Padrón-Navarta for their constructive criticism on the earlier version of the manuscript.

REFERENCES

- Akbulut M., Pişkin Ö., Karayiğit A.İ., 2006. The genesis of the carbonatized and silicified ultramafics known as listvenites: a case study from the Mihaliççık region (Eskişehir), NW Turkey. *Geological Journal*, 41: 557-580.
- Aminu M.D., Nabavi S.A., Rochelle C.A., Manovi V., 2017. A review of developments in carbon dioxide storage. *Applied Energy*, 208: 1389-1419.
- Aydal D., 1989. Gold-bearing listwaenites in the Araç Massif, Kastamonu, Turkey. *Terra Nova*, 2: 43–52.
- Balci N., Gunes Y., Kaiser K., Akcer On S., Eris K., Garczynski B., Horgan B.H.N., 2020. Biotic and abiotic imprints on Mg-rich stromatolites: Lessons from Lake Salda, SW Turkey. *Geomicrobiology Journal*, 37 (5): 401-425. <https://doi.org/10.1080/01490451.2019.1710784>.
- Beinlich A., Austrheim H., 2012. In situ sequestration of atmospheric CO₂ at low temperature and surface cracking of serpentinized peridotite in mine shafts. *Chemical Geology*, 332–333: 32–44. <http://dx.doi.org/10.1016/j.chemgeo.2012.09.015>.
- Beinlich A., Plümper O., Boter E., Müller I.A., Kourim F., Ziegler M., Harigane Y., Lafay R., Kelemen P.B., Oman Drilling Project Science Team, 2020. Ultramafic rock carbonation: Constraints from listvenite core BT1B, Oman drilling project. *Journal of Geophysical Research: Solid Earth*, 125: e2019JB019060. <https://doi.org/10.1029/2019JB019060>.
- Bethke C.M., Yeakel S., 2007. *The Geochemist's Workbench®2023, Community Edition, GWB Essentials Guide*, Hydrogeology Program, University of Illinois, Urbana, Illinois.
- Blunden J., Arndt D. S. 2019. State of the climate in 2018. *Bull. Am. Meteorol. Soc.*, 100: S1–S305.
- Boschi C., Dini A., Dallai L., Ruggieri G., Gianelli G., 2009. Enhanced CO₂-mineral sequestration by cyclic hydraulic fracturing and Si-rich fluid infiltration into serpentinites at Malenrata (Tuscany, Italy). *Chemical Geology*, 265: 209-226, doi:10.1016/j.chemgeo.2009.03.016.
- Boschi C., Dini A., Baneschi I., Bedini F., Perchiazzi N., Cavallo A., 2017. Brucite-driven CO₂ uptake in serpentinized dunites (Ligurian Ophiolites, Montecastelli, Tuscany). *Lithos*, 288-289: 264-281. <http://dx.doi.org/10.1016/j.lithos.2017.07.005>
- Boztuğ D., Larson L.T. , Yılmaz S. , Uçurum A., and Oztürk A., 1994. Geological setting, mineralogy and precious metal content of the listwaenitic rocks in the Alacahan region, SE Sivas, CE Anatolia, Turkey. 15nd year symposium of Faculty of Engineering and Architecture, April, 4-7, 1994 Adana, Turkey. *J. of Faculty of Engineering and Architecture, Çukurova University*, special issue: 163-177.
- Braithwaite C.J.R., Zedef V., 1996. Hydromagnesite stromatolites and sediments in an alkaline lake, Salda Gölü, Turkey. *Journal of Sedimentary Research*, 66 (5): 991–1002.
- Çiftçi Y., 1998. Metalogeny of the ophiolites in İmranlı-Refahiye area. Symposium of 20th anniversary of education of geological engineering in Fırat University on 75th anniversary of the Republic of Turkey, abstract: 91.
- Ercan T., 1982. Kula yöresinin jeolojisi ve volkanitlerin petrolojisi. *İstanbul Yerbilimleri Dergisi*, 3 (1-2): 77-124.
- Ercan T., Günay E., Dinçel A., Türkecan A., Küçükayman A., 1980. Kula-Selendi yörelerinin jeolojisi ve volkanitlerin petrolojisi. MTA Raporu No. IV/01.0.01.07.02. (in Turkish)

- Erler A., Larson L.T., 1990. Genetic classification of gold occurrences of the Aegean region of Turkey. In: M.Y. Savaşçın, A.H. Eronat (Eds). Proceedings of the International Earth Sciences Congress on the Aegean Regions, 1990, October 1-6, 1990, İzmir-Turkey, Dokuz Eylül University, IESCA Publications, 2: p. 12–23.
- Frost B.R., Beard J.S., 2007. On silica activity and serpentinization. *Journal of Petrology*, 48:1351-1368. <https://doi.org/10.1093/petrology/egm021>.
- Gautier Q., Bénézech P., Mavromatis V., Schott J., 2014. Hydromagnesite solubility product and growth kinetics in aqueous solution from 25 to 75 °C. *Geochimica et Cosmochimica Acta*, 138:1–20. <http://dx.doi.org/10.1016/j.gca.2014.03.044>.
- Genç Y., Gorzawski H., Amstutz G.C., 1990. Silica-carbonate-talc alteration of the serpentinite from the Narman Karadag ophiolitic complex (Erzurum-Turkey): Its mineral paragenesis and chemistry. In: M.Y. Savaşçın, A.H. Eronat (Eds). Proceedings of the International Earth Sciences Congress on the Aegean Regions, 1990, October 1-6, 1990, İzmir-Turkey, Dokuz Eylül University, IESCA Publications, 1: p. 246-255.
- Giampouras M., Garrido C.J., Bach W., Los C., Fussmann D., Monien P., García-Ruiz J.M., 2020. On the controls of mineral assemblages and textures in alkaline springs, Samail Ophiolite, Oman. *Chemical Geology*, 533: 119435. <https://doi.org/10.1016/j.chemgeo.2019.119435>
- Gültekin A.S., 1993, The geology of the area between Alacahan-Çetinkaya and Divriği (Sivas Province). Unpublished Ph.D. Thesis. İstanbul University, 183 pp. (Turkish with English abstract).
- Grützner T., Prelevic D., Akal C., 2013. Geochemistry and origin of ultramafic enclaves and their basanitic host rock from Kula Volcano, Turkey. *Lithos*, 180-181:58-73. <https://doi.org/10.1016/j.lithos.2013.08.001>
- Hamilton W.J., Strickland H.E., 1841. On the geology of the western part of Asia Minor. *Trans. Geol. Soc. Lond.*, 6: 1–39.
- Hofmeister A.M., Chopelas A., 1991. Vibrational spectroscopy of end-member silicate garnets. *Phys. Chem. Miner.*, 17: 503–526.
- Holm N.G., Oze C., Mousis O., Waite J.H., Guilbert-Lepoutre A., 2015. Serpentinization and the Formation of H₂ and CH₄ on celestial bodies (Planets, Moons, Comets). *Astrobiology*, 15 (7): 587-599. doi: 10.1089/ast.2014.1188.
- Hopkinson L., Kristova P., Rutt K., Cressey G., 2012. Phase transitions in the system MgO–CO₂–H₂O during CO₂ degassing of Mg-bearing solutions. *Geochimica et Cosmochimica Acta*, 76:1–13. <http://dx.doi.org/10.1016/j.gca.2011.10.023>.
- Hostetler P.B., 1960. Low temperature relations in the system: MgO-SiO₂-CO₂ H₂O. Ph.D. diss., Harvard Univ., Cambridge, Mass.168 pp.
- Hostetler P.B., Coleman R.G., Mumpton F.A., Evans B.W., 1966. Brucite in Alpine serpentinites. *American Mineralogist*, 51: 75-98.
- Kelemen P.B., Matter J., Streit E.E., Rudge J.F., Currey W.B., Blusztajn J., 2011. Rates and mechanisms of mineral carbonation in peridotite: Natural processes and recipes for enhanced, in-situ CO₂ capture and storage. *Annu. Rev. Earth Planet. Sci.*, 39:545-576.
- Kelemen P.B., McQueen N., Wilcox J., Renforth P., Dipple G., Vankeuren A.P., 2020. Engineered carbon mineralization in ultramafic rocks for CO₂ removal from air: Review and new insights. *Chemical Geology*, 550: <https://doi.org/10.1016/j.chemgeo.2020.119628>.
- Kılıç G., Aydoğan M.S., Kumral M., 2018. Preliminary results of the radiolarian-chert hosted manganese deposit within the Vezirler ophiolitic mélange (Kula-Manisa, western Turkey): constraints on the origin, paleo-redox conditions, and depositional environments. *Arabian Journal of Geosciences*, 11: 628. <https://doi.org/10.1007/s12517-018-3984-6>.
- Klein F., Garrido C.J., 2011. Thermodynamic constraints on mineral carbonation of serpentinized peridotite. *Lithos* 126 (3–4): 147–160. <http://dx.doi.org/10.1016/j.lithos.2011.07.020>.
- Koç Ş, Kadioğlu Y.K., 1996. Mineralogy, geochemistry and precious metal content of Karacakaya (Yunussemre-Eskişehir) listwaenites. *Ofioliti*, 21: 125–130.

- Königsberger E., Königsberger L.-C., Gamsjäger H., 1999. Low-temperature thermodynamic model for the system $\text{Na}_2\text{CO}_3\text{--MgCO}_3\text{--CaCO}_3\text{--H}_2\text{O}$. *Geochimica et Cosmochimica Acta*, 63: 3105–3119.
- Lackner, K.S., Wendt, C.H., Butt, D.P., Joyce, E.L., Sharp, D.H., 1995. Carbon dioxide disposal in carbonate minerals. *Energy*, 20 (11): 1153–1170.
- Laetsch T., Downs R., 2006. Software for identification and refinement of cell parameters from powder diffraction data of minerals using the RRUFF project and American Mineralogist Crystal Structure Databases. 19th General Meet. Intern. Miner. Ass., Kobe, Japan, July 2006. Abstr.: 23-28
- Larson L.T., Erler A., 1992. Geologic setting and geochemical signatures of twenty-two precious metal prospects in Turkey. *Yerbilimleri/Geosound*, 20: 9–28.
- Legros G., 1969. Contribution a l'etude geologique et Metallogenique de la region de Divrigi (Sivas, Turquie). Unpublished Ph.D. thesis, Science and Technology University of Montpellier, France, 58 pp.
- Leo G.H., Önder E., Kılıç M., Avcı M., 1978. Geology and mineral resources of the Kuluncak-Sofular area (Malatya, K-39a1 and K-39a2 quadrangles), Turkey. *U.S. Geological Survey Bull.*, 1429: 58 pp.
- Mumpton F.A., Thompson C.S., 1966. The stability of brucite in the weathering zone of the New Idria serpentinite. *Clays and Clay Minerals*, 14: 249-257.
- Oelkers E.H., Gislason S.R., 2023. Carbon capture and storage: From global cycles to global solutions. *Geochemical Perspectives*, 12(2): 179-349. doi: 10.7185/geochempersp.12.2
- Oygür V., Erler A., 1999. Comparison of epithermal and base-metal mineralizations along the Simav graben. In: R. Ulusay, T. Topal (Eds.) *Proceedings of the 52nd Geological Congress of Turkey*, 10-12 May 1999, Ankara (in Turkish with English abstract): p. 129-136.
- Parkhurst D.L., Appelo C.A.J., 1999. User's guide to PHREEQC (version 2) — a computer program for speciation, batch-reaction, one-dimensional transport and inverse geochemical calculation. *U.S. Geol. Surv. Water-Resources Investigations*, 326.
- Pokrovsky O.S., Schott J., 2004. Experimental study of brucite dissolution and precipitation in aqueous solutions: surface speciation and chemical affinity control. *Geochimica et Cosmochimica Acta*, 68:31–45. [http://dx.doi.org/10.1016/S0016-7037\(03\)00238-2](http://dx.doi.org/10.1016/S0016-7037(03)00238-2).
- Power I.M., Wilson S.A., Dipple G.M., 2013. Serpentinite carbonation for CO_2 sequestration. *Elements*, 9: 115-121. <https://doi.org/10.2113/gselements.9.2.11>
- Power I.M., Wilson S.A., Thorn J.M., Dipple G.M., Gabites J.E., Southam G., 2009. The hydromagnesite playas of Atlin, British Columbia, Canada: A biogeochemical model for CO_2 sequestration. *Chemical Geology* 260: 286–300, doi:10.1016/j.chemgeo.2009.01.012.
- Power I.M., Wilson S.A., Harrison A.L., Dipple G.M., Mccutcheon J., Southam G., Kenward P.A., 2014. A depositional model for hydromagnesite–magnesite playas near Atlin, British Columbia, Canada. *Sedimentology*, 61: 1701-1733, doi: 10.1111/sed.12124.
- Reçber A., Koç Ş., Kadioğlu, Y.K., 1997. Geochemical and geostatistical determination of Yunusemre (Eskişehir) listwaenite. In: *Symposium of 20th Anniversary of Education of Geological Engineering in Çukurova University*, Abstracts, p. 132.
- Richardson-Bunbury J.M., 1996. The Kula volcanic field, western Turkey: the development of a Holocene alkali basalt province and the adjacent normal-faulting graben. *Geol. Mag.*, 133: 275–283.
- Scheller E.L., Swindle C., Grotzinger J., Barnhart H., Bhattacharjee S., Ehlmann B., Farley K., Ficher W.W., Greenberger R., Ingalls M., Martin P.E., Osorio-Rodrigues D., Smith B.P., 2021. Formation of magnesium carbonates on Earth and implications for Mars. *J Geophys Res Planets*, 126: e2021JE006828, <https://doi.org/10.1029/2021JE006828>.
- Smith W., 1854. *Dictionary of Greek and Roman Geography*, illustrated by numerous engravings on wood. London. Walton and Maberly, Upper Gower Street and Ivy Lane, Paternoster Row; John Murray, Albemarle Street.

- Snow, J.E., Dick, H.J.B., 1995. Pervasive magnesium loss by weathering of peridotite. *Geochimica et Cosmochimica Acta* 59:4219–4235. [http://dx.doi.org/10.1016/0016-7037\(95\)00239-V](http://dx.doi.org/10.1016/0016-7037(95)00239-V).
- Snæbjörnsdóttir S.Ó., Sigfússon B., Marieni C., Goldberg D., Gislason S.R., Oelkers E.H., 2020. Carbon dioxide storage through mineral carbonation. *Nature Reviews Earth & Environment*, 1: 90–102. <https://doi.org/10.1038/s43017-019-0011-8>.
- Stamatakis M.G., Mitsis I., 2013. The occurrences of Mg-hydroxycarbonates in serpentinites of the western section of the South Aegean volcanic arc (West Attica peninsula-Northeastern Argolis peninsula), Greece. *Bulletin of the Geological Society of Greece*, 47: 427-437.
- Štubňa J., Bačík P., Fridrichova J., Hanus R., Illášová L., Milovská S., Škoda R., Vaculovič T., Čerňanský S., 2019. Gem-Quality Green Cr-Bearing Andradite (var. Demantoid) from Dobšiná, Slovakia. *Minerals* 9, 164: doi:10.3390/min9030164.
- Tokçaer M., 2000. Geochemistry of Kula Geothermal Area. Dokuz Eylül University, MSc thesis, İzmir, p 122.
- Tokçaer M., Agostini S., Savaşçın M.Y., 2005. Geotectonic setting and origin of the youngest Kula volcanics (Western Anatolia), with a new emplacement model. *Turkish Journal of Earth Sciences*, 14: 145–166.
- Tüysüz N., Erler A., 1993. Geochemistry and evolution of listwaenites in the Kağızman region (Kars, NE-Turkey). *Chemie der Erde*, 53: 315–329.
- Uçurum A., 1996. Geology, Geochemistry and Mineralization of the Silica-Carbonate Alteration (Listwaenite) from Late Cretaceous Ophiolitic Melanges at Cürek-Divriği in Sivas Province and at Güvenç, Karakuz-Hekimhan in Malatya Province, Central East Turkey. Ph. D. Thesis, University of Nevada Reno, USA [unpublished].
- Uçurum A., 2000. Listwaenites in Turkey: perspectives on formation and precious metal concentration with reference to occurrences in East-Central Anatolia. *Ofioliti*, 25: 15–29.
- Uçurum A., Larson L.T., 1999. Geology, base-precious metal concentration and genesis of the silica-carbonate alteration (listwaenites) from late Cretaceous ophiolitic mélanges at Cürek-Divriği in Sivas province and at Güvenç, Karakuz-Hekimhan in Malatya province, central east Turkey. *Chemie der Erde Geochemistry*, 59: 77–104.
- Wilson M.J., 2014. The structure of opal-CT revisited. *Journal of Non-Crystalline Solids*, 405: 68-75. <http://dx.doi.org/10.1016/j.jnoncrysol.2014.08.052>.
- Yavuz H., Demir Y., Kasapçı C., Uysal İ., Helvacı C., 2022. Geology and genesis of the silica-listwaenite hosted Kaymaz gold deposit, Eskişehir, NW-Turkey: Implications from fluid inclusions and pyrite chemistry. *Journal of Asian Earth Sciences*:X, <https://doi.org/10.1016/j.jaesx.2022.100104>
- Yıldızeli N., Yurt M.Z., Yıldırım A., Adıgüzel O., Avcı N., Çubuk Y., 1987. Geological report on iron exploration around Kangal-Alacahan (Sivas) and Kuluncak (Malatya) regions. MTA report, no: 8176, 29 pp. (in Turkish).
- Zedef V., Russell M.J., Fallick E., 2000. Genesis of vein stockwork and sedimentary magnesite and hydromagnesite Deposits in the ultramafic terranes of southwestern Turkey: A stable isotope study. *Economic Geology*, 95: 429-446.
- Zhang P-C., Anderson H.L.Jr., Kelly J.W., Krumhansl J.L., Papenguth H.W., 2000. Kinetics and Mechanisms of Formation of Magnesite from Hydromagnesite in Brine. Office of Scientific & Technical Information Technical Reports (OSTI), Report No. SAND99-1946J, 24 p., ark:/67531/metadc717954.

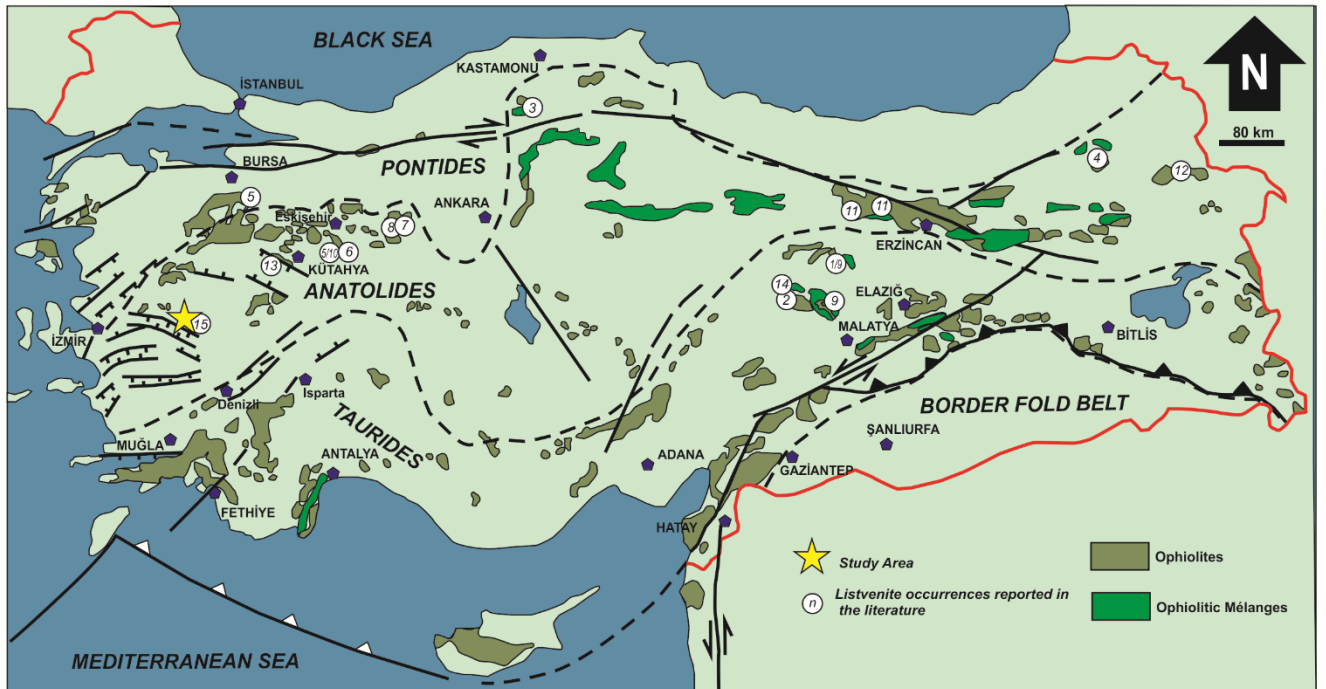


Fig. 1. Locations of the listvenites described from the serpentinites and serpentinite-matrix mélanges of northern and eastern Turkish ophiolites. The location of the study area is shown with a yellow star. Fig. modified after Uçurum (2000). Listvenite locations are from: (1) Legros (1969), (2) Leo et al. (1978); Yıldızeli et al. (1987), (3) Aydal (1989), (4) Genç et al. (1990), (5) Eler and Larson (1990); Larson and Eler (1992), (6) Yavuz et al. (2022), (7) Akbulut et al. (2006), (8) Koç and Kadioğlu (1996), (9) Uçurum (1996); Uçurum and Larson (1999), (10) Reçber et al. (1997), (11) Çiftçi (1998), (12) Tüysüz and Eler (1993); (13) Oygür and Eler (1999), (14) Gültekin (1993); Boztuğ et al. (1994), and (15) Ercan (1982).

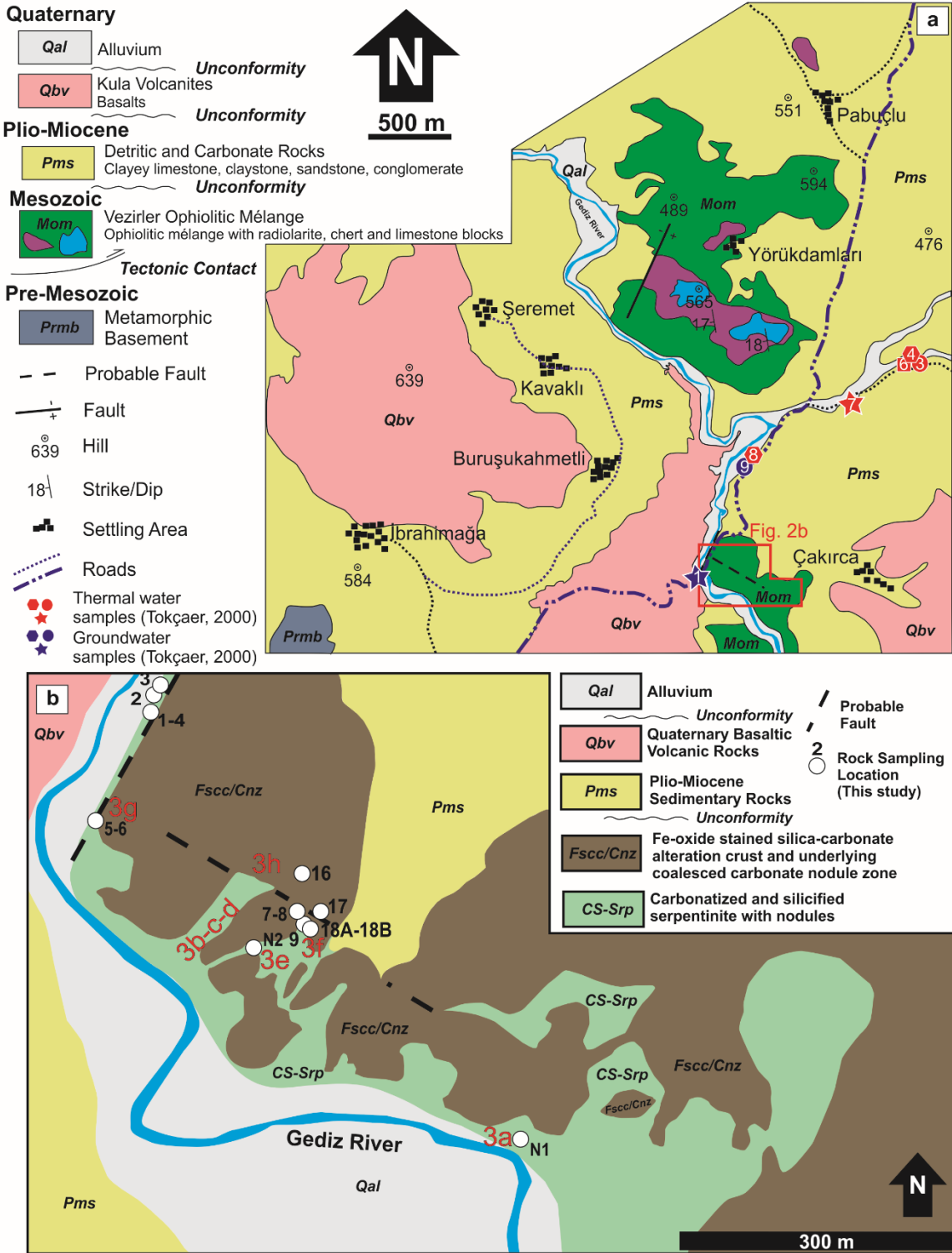


Fig. 2. (a) Geological map of northeast of Kula (modified after Ercan et al., 1980; Kılıç et al., 2018). Inset shows location of Fig. 2b. Locations of the thermal and ground water samples are from Tokçaer (2000). (b) Detailed geological map of the studied outcrop and surroundings created via field observations and satellite imagery. White circles mark the sampling locations. Red coloured scripts denote the field imaging locations given in Fig. 3.

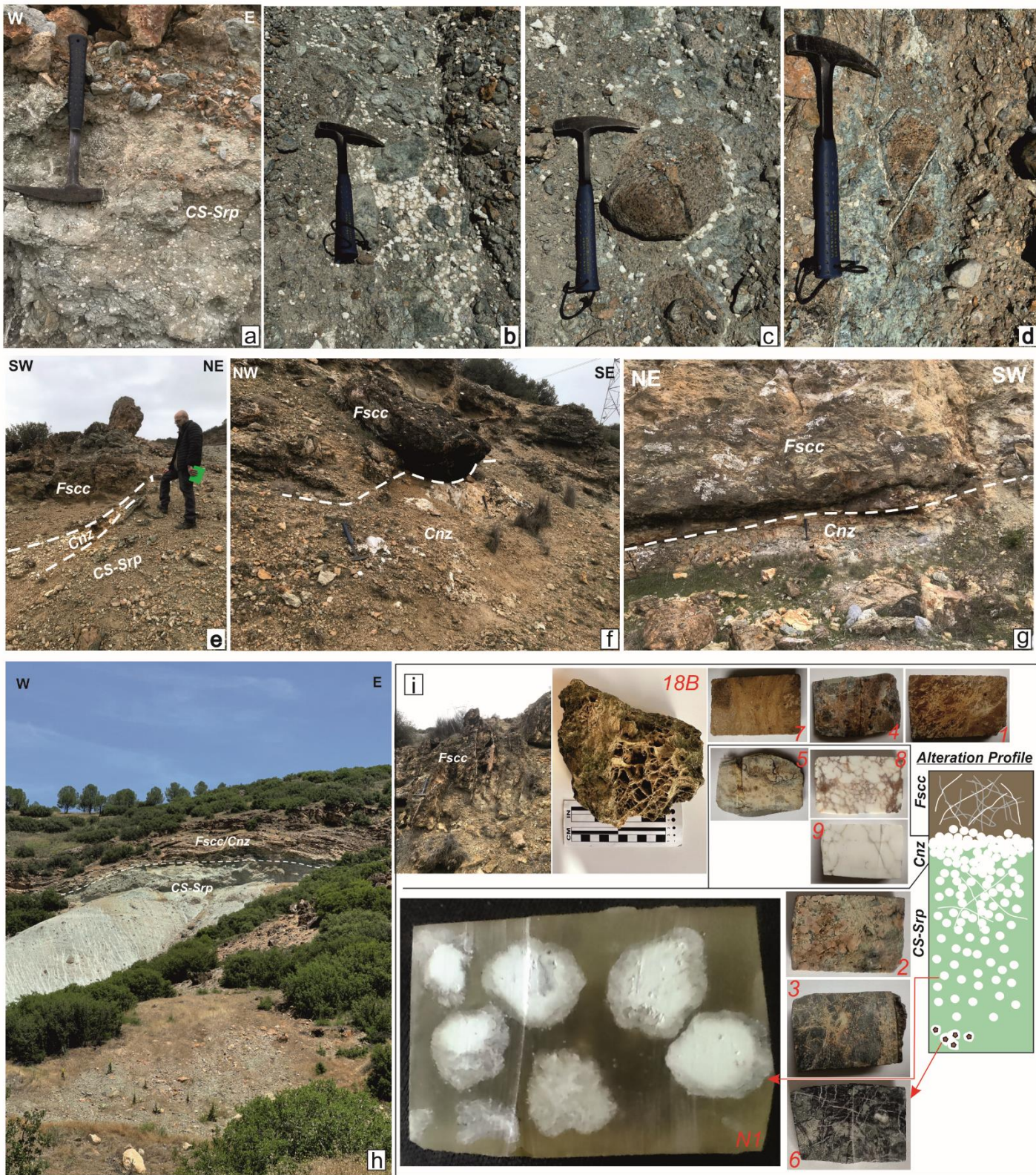


Fig. 3. Field images from the alteration profile. (a-d) show white carbonate nodules and veinlets in carbonatized and silicified serpentinite (CS-Srp). (e-h) show the primary contacts of the three different segments of the alteration profile; from top to bottom: iron-oxide stained silica-carbonate alteration crust (Fsc), coalesced carbonate nodule zone (Cnz), and the carbonatized and silicified serpentinite (CS-Srp). (i) shows a simplified columnar section illustrating the relation of the segments of the alteration profile and field/hand specimen images exemplifying the macroscopic visuals of the alteration products.

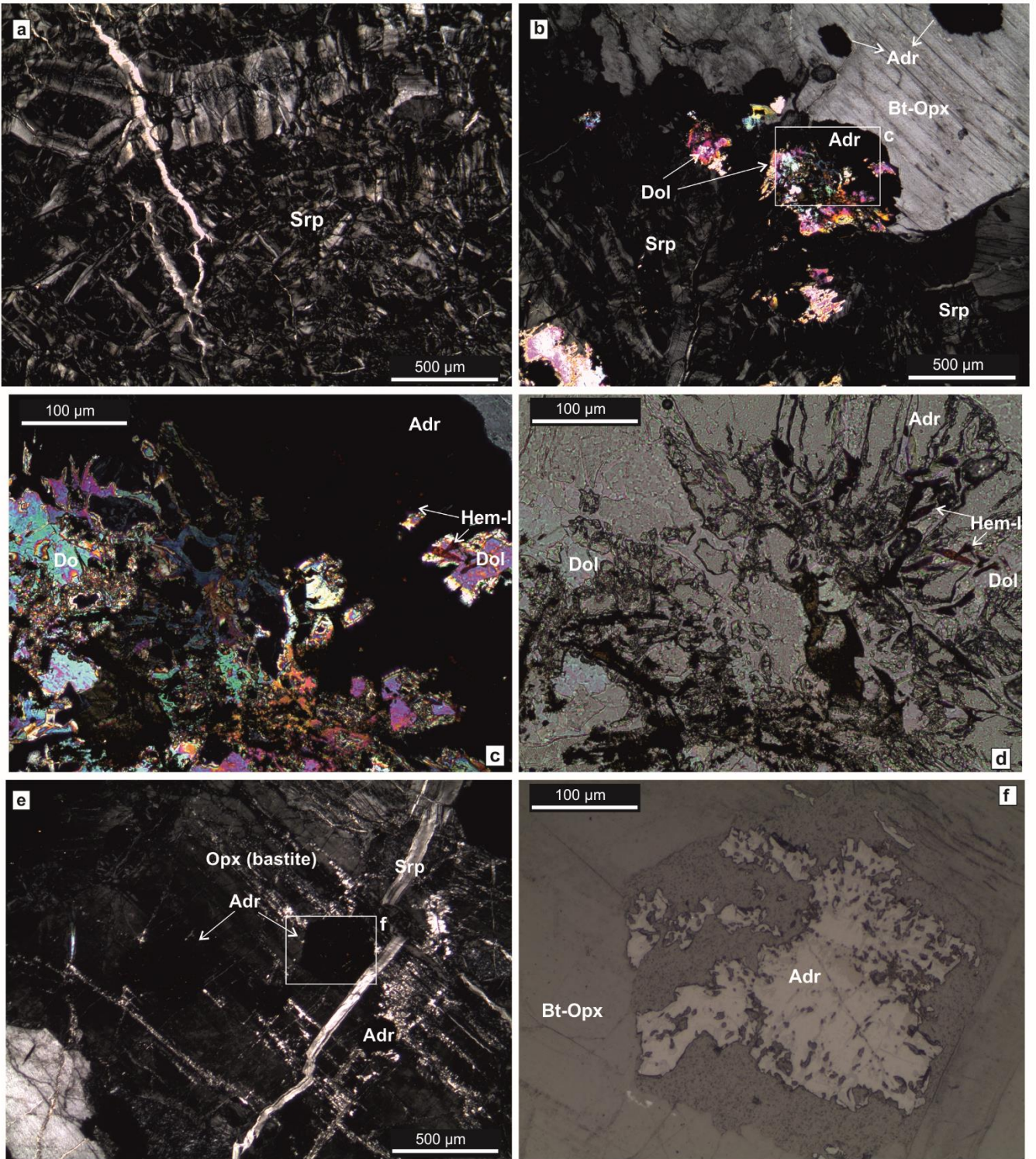


Fig. 4. (a-f) Microphotographs of the carbonatized and silicified serpentinite (CS-Srp). (a), (b), (c) and (e) are under transmitted light and crossed nicols (+N), (d) is under parallel nicols (//N), and f is under reflected light and //N, air immersion conditions. Srp: serpentine, And: andradite, Do: dolomite, Opx (bastite): bastite transformed orthopyroxene; Hmt-I: hematite-I.

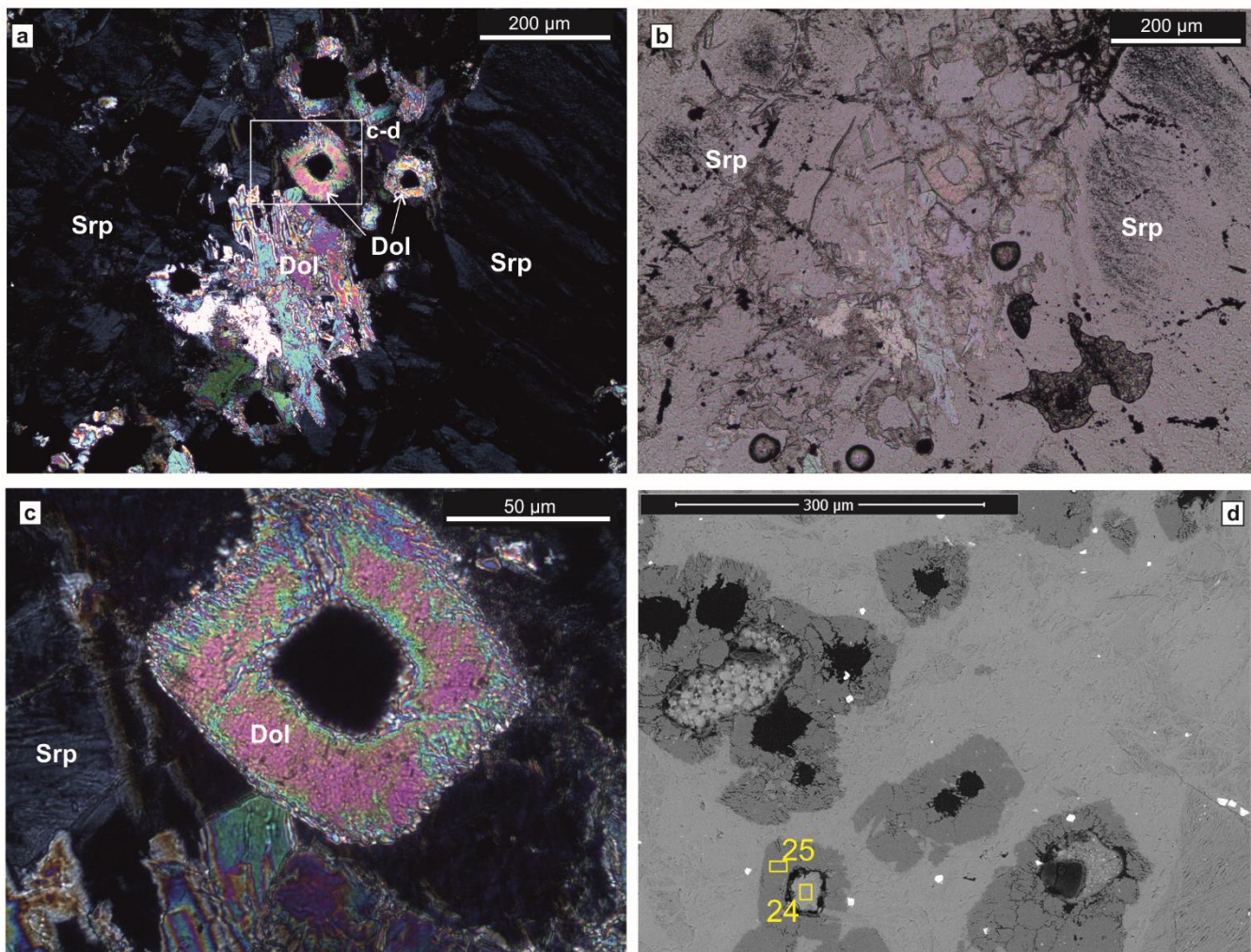


Fig. 5. (a-c) Microphotographs of the leftover voids encircled by dolomite coronas in some parts of the serpentine mesh matrix under transmitted light. (a) and (c) are under +N, (b) is under //N. (d) Back-scattered Electron Image (BSE) of the leftover voids and intact grains encircled by dolomite coronas. Yellow squares illustrate areas of interest studied via EDS (see Supplementary Fig. 2S).

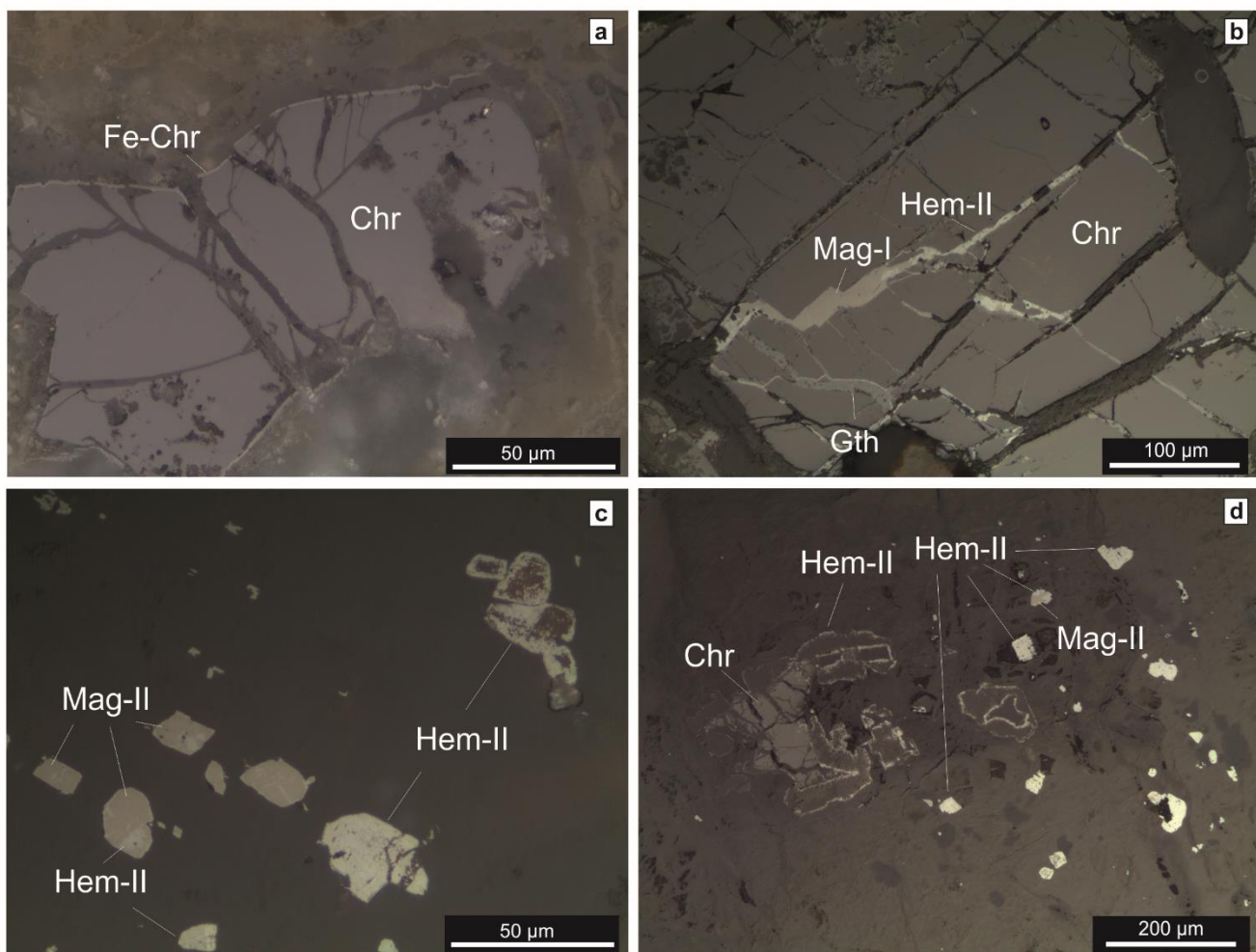


Fig. 6. (a-d) Microphotographs of the opaque phases in serpentinites under reflected light (//N, air immersion). Chr: chromite, Fe-Chr: ferrite-chromite, Mag-I: magnetite-I, Mag -II: magnetite-II, Hem-II: hematite-II, Gth: goethite.

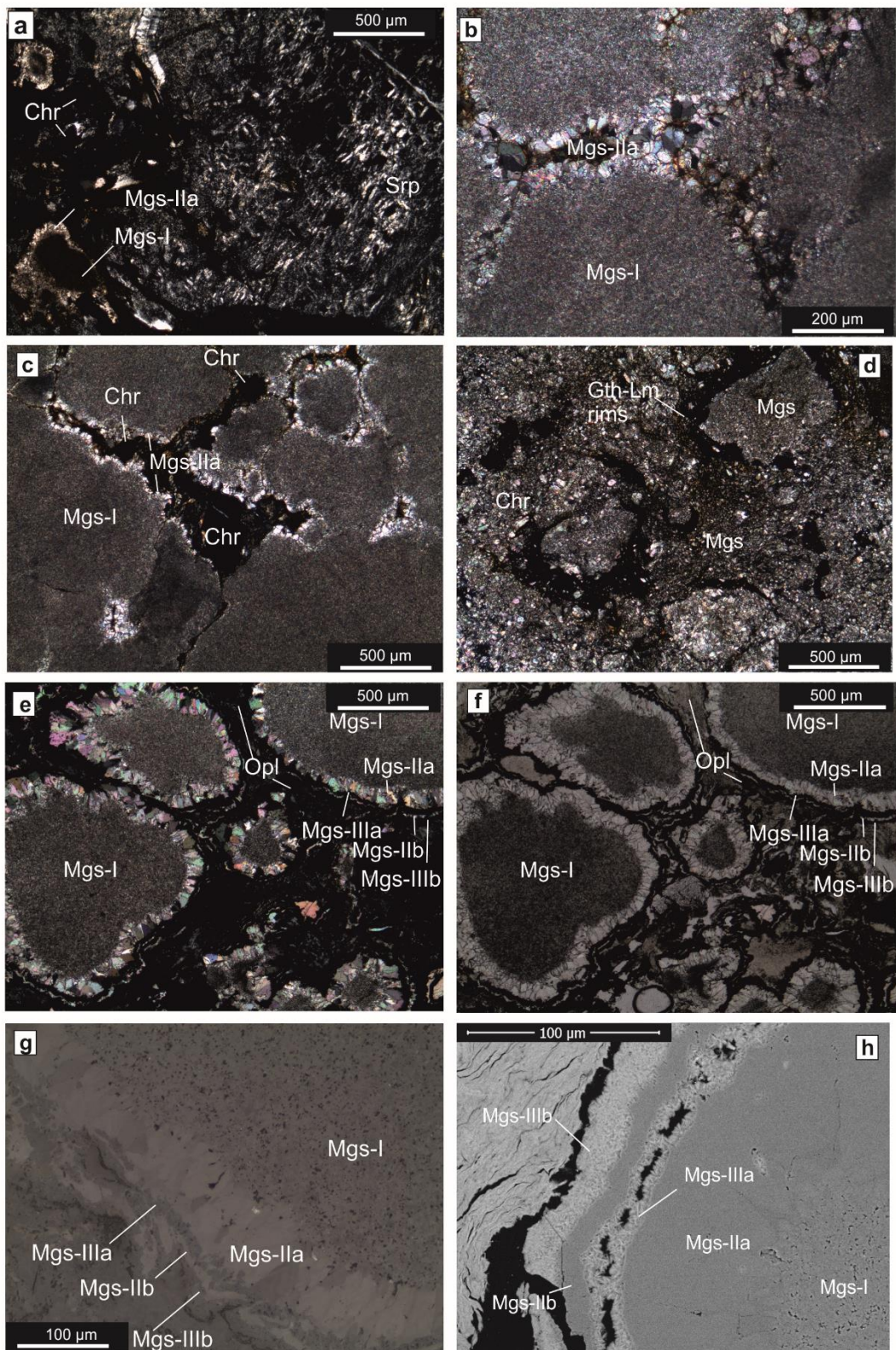


Fig. 7. (a-f) Microphotographs of the carbonate nodules sampled from and immediate vicinity below the Cnz. (a-e) are under transmitted light and +N, (f) is under //N, and g is under reflected light and //N, air immersion conditions. (h) Back-scattered Electron Image (BSE) of a magnesite nodule. A ubiquitous textural zoning from core to rim is distinctive. Chr: chromite, Srp: serpentine, Mgs: magnesite, Mgs-I: magnesite-I, Mgs-IIa: magnesite-IIa, Mgs-IIIa: magnesite-IIIa, Mgs-IIb: magnesite-IIb, Mgs-IIIb: magnesite-IIIb, Gth-Lm: goethite-limonite, Opl: Opal.

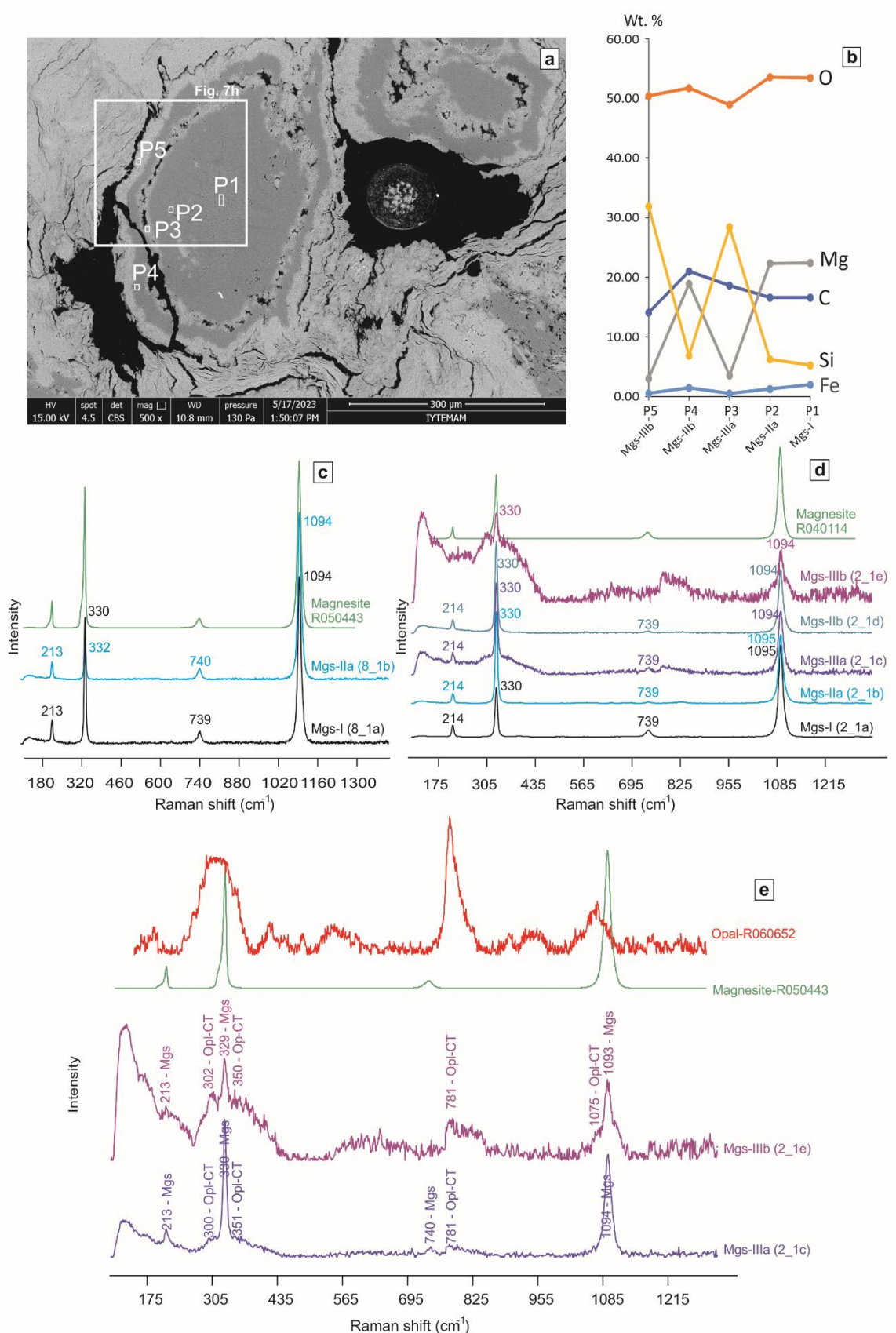


Fig. 8. (a) A zoom-out BSE image of nodule presented in Fig. 7h (area of Fig. 7h is shown with a white inset). White squares coded with white scripts are the areas of interest for the EDS analysis. (b) Elemental variations along the points given in Fig. 8a. (c) Raman spectra of the fine-grained -core zones. (d) Raman spectra of the coarse-grained surrounding zones and magnesite spectra from RRUFF Raman spectral library used for comparison. (e) Raman spectrum from the lattice-bladed magnesite layers shows a composite spectrum revealing coexistence of magnesite and opal-CT at the analysed areas.

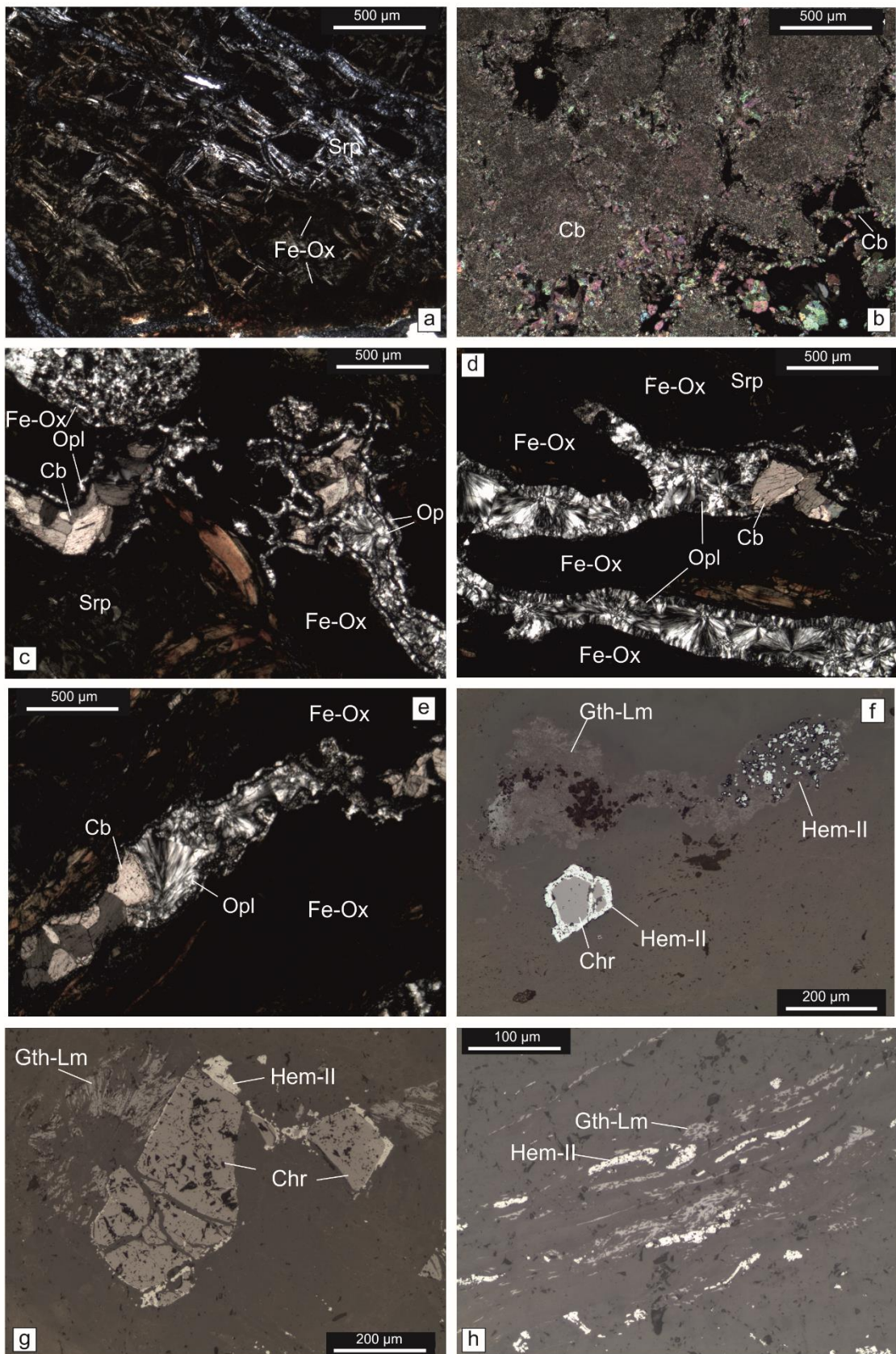


Fig. 9. (a-h) Microphotographs from the uppermost zone of the alteration profile, the iron-oxide stained silica-carbonate alteration crust (Fsc). (a-e) are under transmitted light and +N and (f-h) are under reflected light (//N, air immersion). (a) relict patches of iron-oxide stained serpentine mesh texture in the Fsc. (b) coalesced carbonate nodules in the lower segments of the Fsc. (c-e) Carbonate and silica veinlets cross-cutting the relict serpentine mesh patches in the upper part of the Fsc. (f-h) reflected light microphotographs of the opaque phases in Fsc. Srp: serpentine, Cb: carbonate mineral, Fe-Ox: iron-oxide stain, Opl: opal, Chr: chromite, Hem-II: hematite-II, Gth-Lm: goethite-limonite.

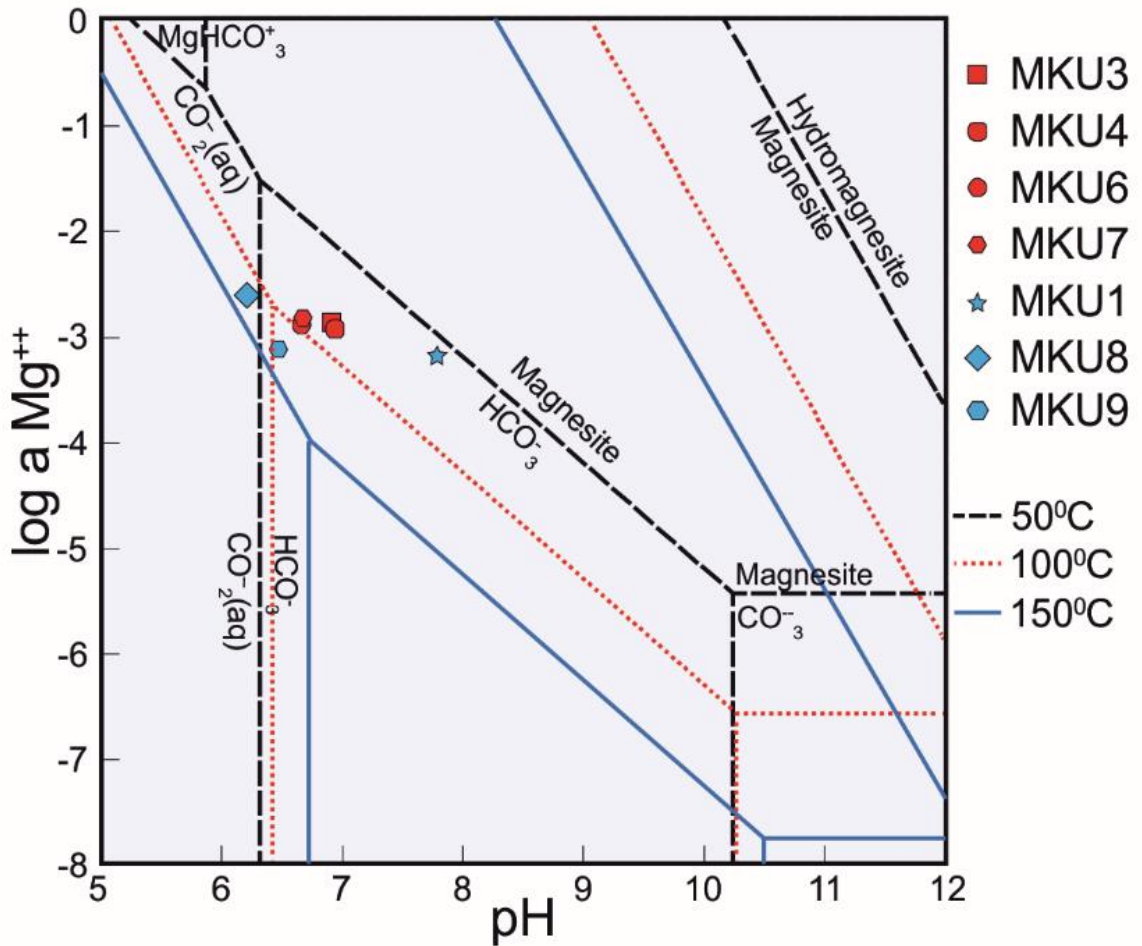


Fig. 10. log aMg⁺⁺ vs. pH plot showing the distribution of the thermal and cold waters from and around the study area. Raw data are from Tokçaer (2000). Sampling locations are shown in Fig. 2. The geochemical modelling software PHREEQC for Windows (version 3.7.3.15968) (Parkhurst and Appelo, 1999) was used for activity calculations. Symbols are as in Fig. 2. Stability fields are drawn as a function of pH and log aMg⁺⁺ for P = 1.013 bar at 50 and 100 °C, and for P = 4.76 bars for 150 °C, and a HCO₃⁻ activity of 10⁻³ using The Geochemist's Workbench®2023 Community Edition (Bethke and Yeakel, 2007). Artinite phase is suppressed in the process in order to obtain the magnesite-hydromagnesite stability line.

Fig. 1S: (a) Laser-Raman spectrum of the andradite. Red spectrum and the code above show andradite data from RRUFF Raman spectral library used for comparison. (b) Electron dispersive spectrometry (EDS) data from andradite grains.

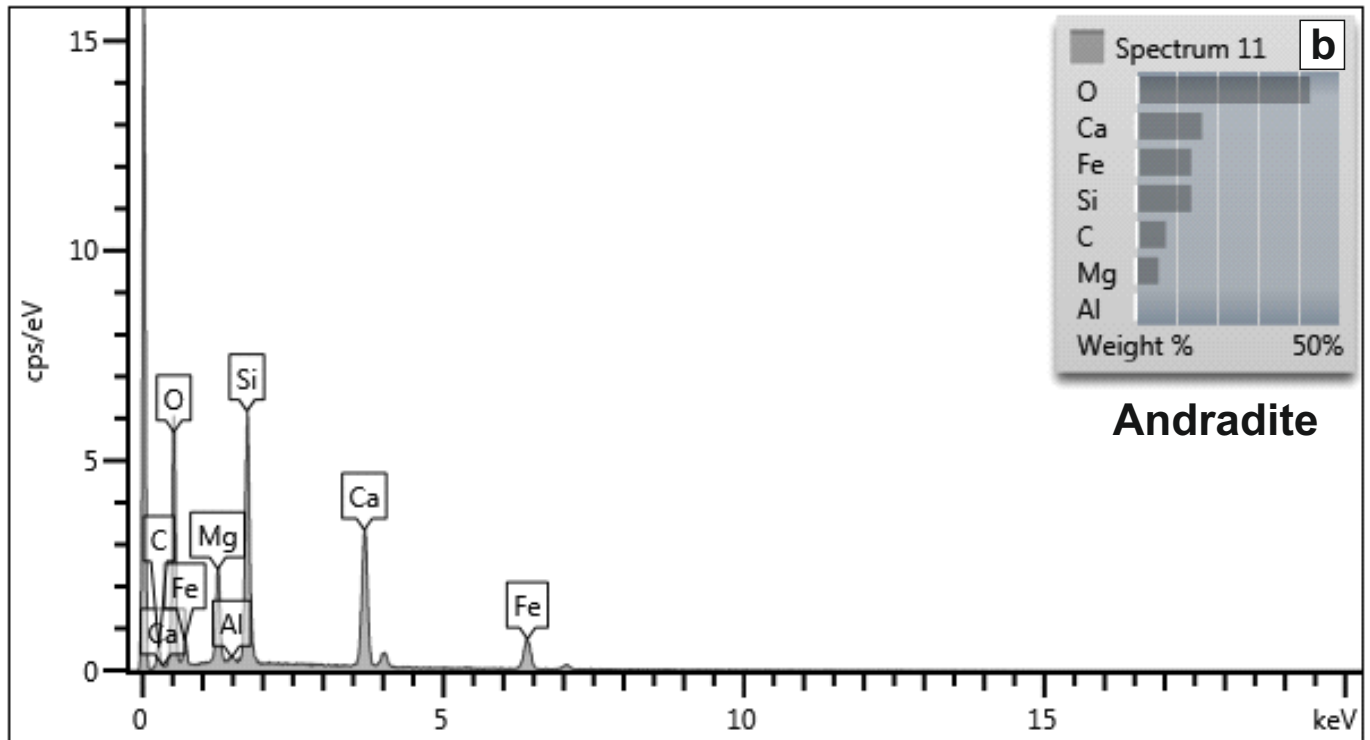
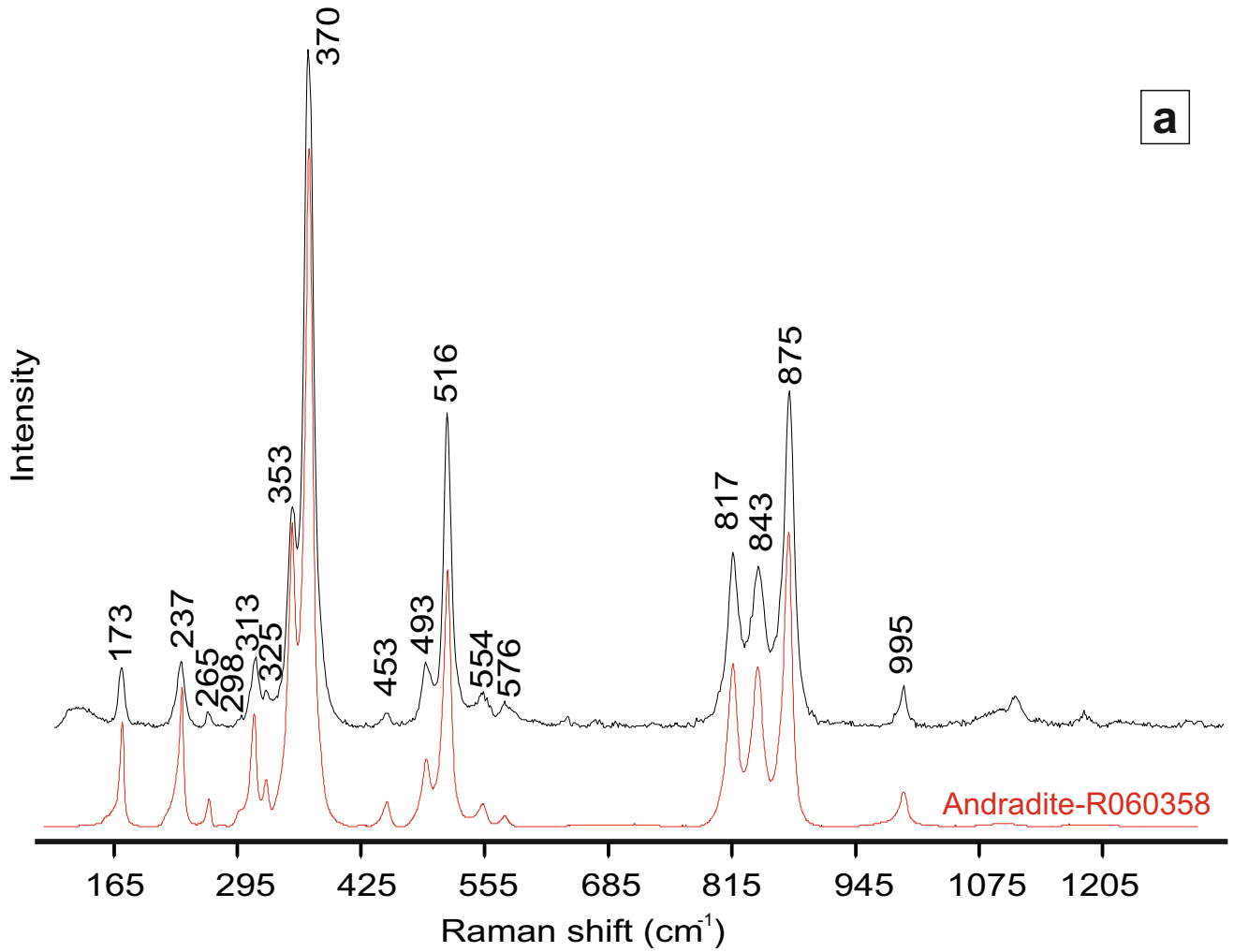


Fig. 2S: (a-b) EDS data from the marked areas in Figure 5d.

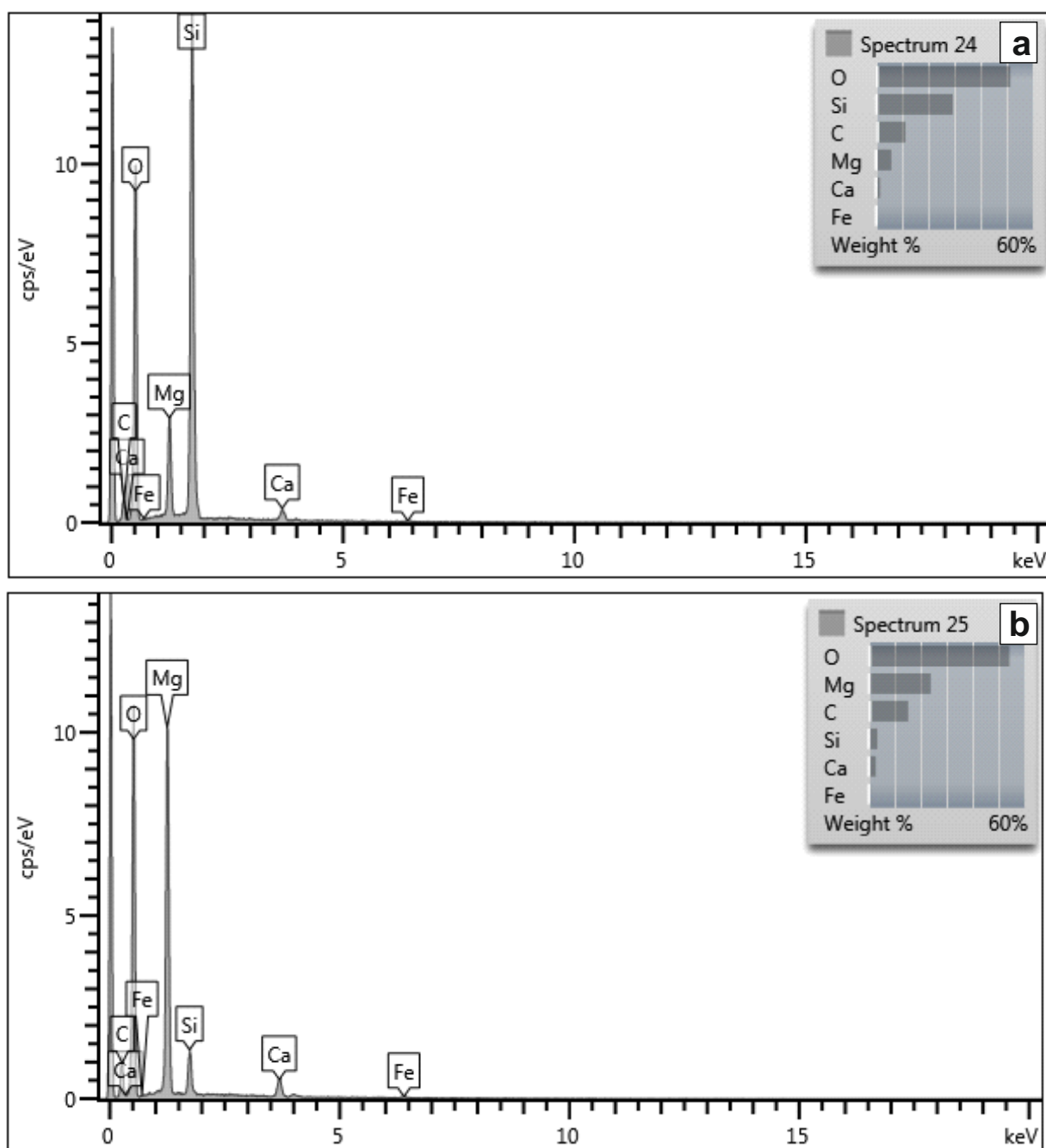


Fig. 3S. (a) Transmitted light microphotograph (//N) of the hydromagnesite $[Mg_5(CO_3)_4(OH)_2 \cdot 4H_2O]$ -hydrotalcite $[Mg_6Al_2(OH)_{16}[CO_3] \cdot 4H_2O]$ and lizardite bearing nodules in the carbonatized and silicified serpentinite (CS-Srp). Red points mark areas of interest studied via EDS. (b and c) Back-scattered Electron Images (BSE) of the areas of interest studied. (d-e) EDS data from the marked areas and, (f) comparison of the elemental variance in these areas. (g) Whole-rock X-Ray diffraction (XRD) pattern obtained from the studied nodule.

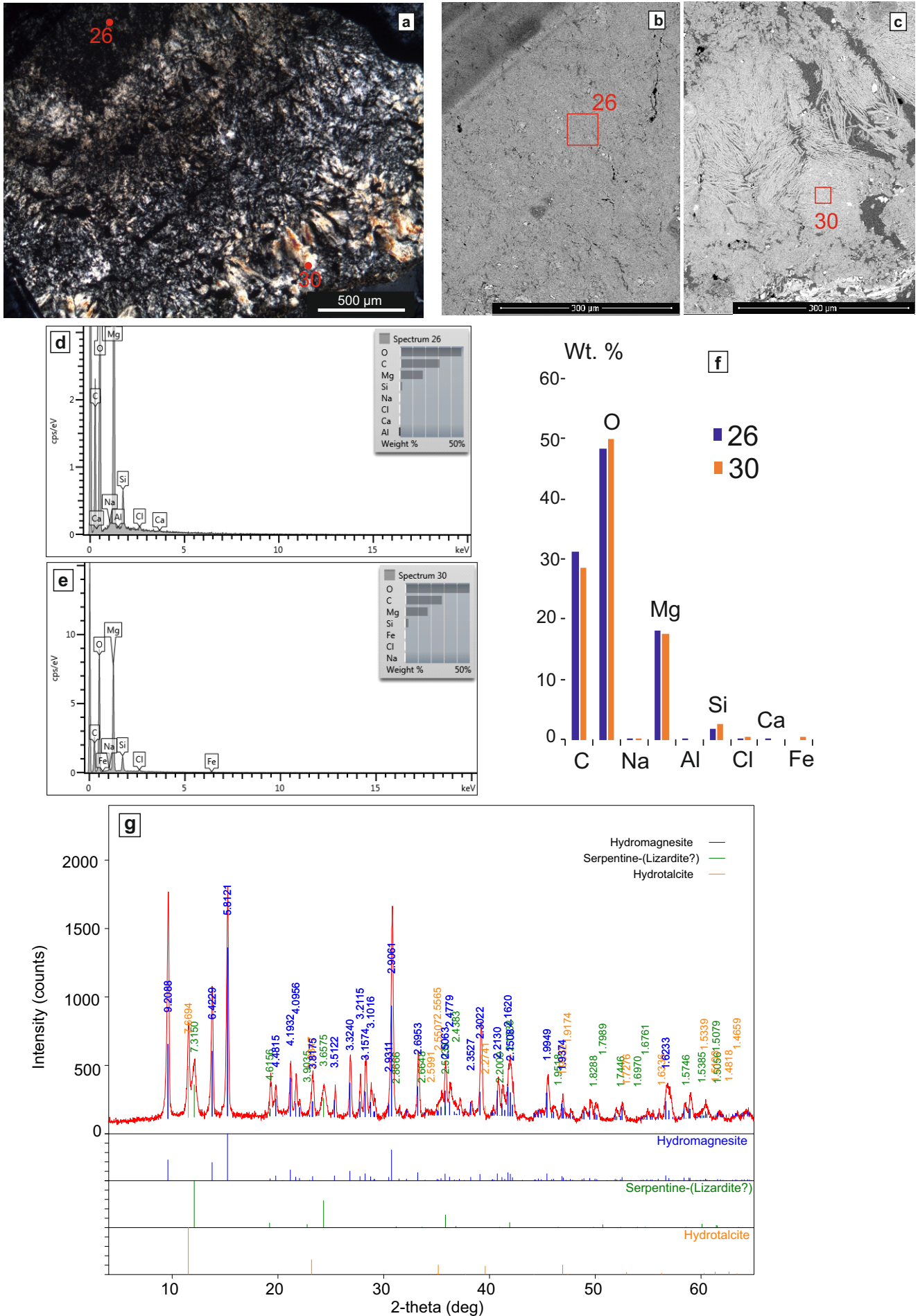


Fig 4S. Whole-rock X-Ray diffraction (XRD) patterns obtained from the lower (a) and upper (b) parts of the iron-oxide stained silica-carbonate alteration crust (Fssc).

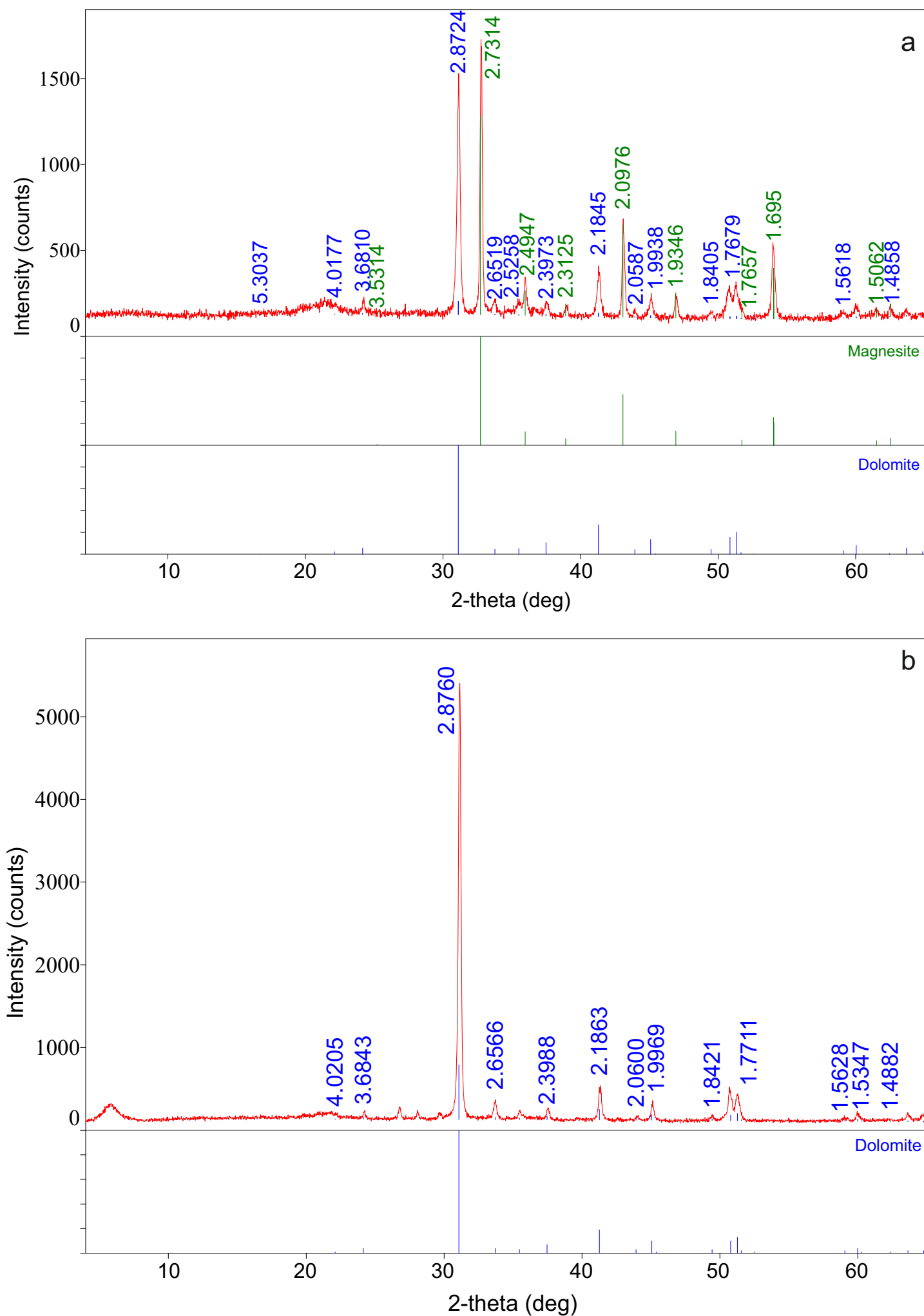


Table 1 - Chemical analysis of geothermal and cold waters from and around the study area. Data from Tokçaer (2000).

<i>Sample</i>	<i>T</i> (°C)	<i>pH</i>	<i>EC</i> (µS/cm)	<i>O₂</i> (mg/l)	<i>Li⁺</i> (mg/l)	<i>Na⁺</i> (mg/l)	<i>K⁺</i> (mg/l)	<i>Mg²⁺</i> (mg/l)	<i>Ca²⁺</i> (mg/l)	<i>Sr²⁺</i> (mg/l)	<i>SiO₂</i> (mg/l)	<i>B</i> (mg/l)	<i>SO₄²⁻</i> (mg/l)	<i>Cl⁻</i> (mg/l)	<i>H₂CO₃</i> (mg/l)	<i>HCO₃⁻</i> (mg/l)	<i>CO₃⁻</i> (mg/l)	<i>TIC as CO₂</i> (mg/l)
1	11.9	7.85	675	9.4	0.02	61.30	42.20	28.90	75.60	<i>n.a.</i>	<i>n.a.</i>	1.65	93.40	150.00	12.40	229.40	0.00	174.30
3	58.9	6.91	4362	1.6	1.32	975.00	106.20	108.80	102.40	0.51	110.00	8.91	104.00	201.00	359.70	3121.60	0.00	2506.80
4	63.1	6.94	4294	1.5	1.32	863.00	105.00	90.90	114.00	0.44	91.00	10.45	104.00	154.00	361.00	2850.70	0.00	2312.20
6	58.7	6.62	4540	0.3	<i>n.a.</i>	982.00	89.40	87.00	58.00	<i>n.a.</i>	120.31	<i>n.a.</i>	112.00	191.00	285.30	2895.10	0.00	2264.70
7	33.1	6.71	4310	3.2	0.92	882.00	88.80	104.00	101.00	0.43	70.00	7.37	152.00	142.00	421.80	2879.30	0.00	2376.00
8	16.8	6.21	3380	0.2	<i>n.a.</i>	268.13	51.00	145.80	270.50	0.29	59.99	1.98	29.10	90.90	740.00	2153.00	0.00	2204.90
9	12.2	6.47	1141	7.5	<i>n.a.</i>	62.00	30.40	32.00	110.00	<i>n.a.</i>	26.06	<i>n.a.</i>	29	109.00	<i>n.a.</i>	478.00	0.00	<i>n.c.</i>

n.a.: not analysed; *n.c.*: not calculated; *TIC as CO₂*: total inorganic carbon as CO₂.